SISSA  ISAS

SCUOLA INTERNAZIONALE SUPERIORE DI STUDI AVANZATI
INTERNATIONAL SCHOOL FOR ADVANCED STUDIES

A first principles study of the thermal expansion in some metallic surfaces

Thesis submitted for the degree of
"Doctor Philosophiæ"

CANDIDATE

Michele Lazzeri

SUPERVISOR

Stefano de Gironcoli

October 1999

Contents

Introduction

In purely harmonic crystals, ionic mean positions do not change upon increasing temperature, thus crystal thermal expansion is a consequence of anharmonic terms in the interatomic potential. Anharmonic effects are expected to be larger at material surfaces than in the bulk, because of the lower symmetry, and as a consequence thermal expansion of a surface is expected to be enhanced.

Recently this subject has attracted much attention, and enhanced thermal effects have been experimentally observed on several surfaces, as, for examples, in: Ni(001) [1], Pb(110) [2], Ag(111) [3], and Be(0001) [4] surfaces. However in some cases the situation is still debated, not only because interpretation of experimental measurements is not sraightforward, but also because of contrasting theoretical results, as for example, for the Ag(111) surface [5]. Finally while good agreement between static calculations and experiment is generally found for low temperature structures, some systems have been singled out in which the inclusion of thermal effects seems to be important even to interpret data taken at room temperatue, as in Be(0001) [4], and Rh(001) [6] surfaces.

Nowadays the equilibrium structure of a large class of materials can be determined theoretically with great accuracy, thanks to state of the art first principles computational methods essentially based on Density Functional Theory (DFT)[7, 8]. Furthermore, the study of thermal behaviour from first principles is now at hand also for complex systems, as surfaces, thanks to the availability of adequate computational power and to the development of sophisicated techniques such as Car-Parrinello method [9] or Density Functional Perturbation Theory [10, 11].

Different approaches have been used to study thermal effects within first-principles methods. Essentially they are based on Molecular Dynamic (MD) simulations and Quasi Harmonic Approximation (QHA), other approaches, such as the self-consistent phonon scheme [12], are presently not feasible from first principles. MD simulations account exactly for interatomic potential anharmonicity, but treat ionic degrees of freedom classically, and can give reliable results only near or above Debye temperature, where quantum effects are negligible. Systems that can be simulated, nowadays, typically consist of about a hundred atoms and the time scale of the simulation can reach a few picoseconds. The knowledge of the frequencies of the vibrational modes of a system allows the application of the QHA scheme. It provides a complementary approach, valid at low temperature, for determining the temperature dependence of structural properties. Moreover, the possibility of including vibrational modes calculated at arbitrary wavelengths, should permit the study of more realistic systems.

Quasi harmonic approximation has been widely used in describing bulk thermal prop-

erties and is commonly believed to work rather well for not to high temperature [13, 14], however little is known, up to now, about its usefullness at the surface. The presence of larger anharmonicity than in the bulk could, infact, lead to a failure of this approximation. Furthermore, to apply QHA scheme vibrational frequencies have to be evaluated as a function of the value of the structural parameters describing the system, and up to now, within a first principles approach, QHA has been used to study only systems described by a small number of structural parameters (bulk materials or surfaces in which only one layer is involved in the thermal expansion). The aim of the present work is to assess the validity of QHA in the study of surface thermal expansion, and to extend this scheme to systems more complex than those studied so far.

Vibrational frequencies can be computed exactly in every point of the Brillouin Zone thanks to Density Functional Perturbation Theory (DFPT) [10, 11]. However, in order to study efficiently systems described by a large number of parameters, it is necessary to calculate the derivative of the vibrational frequencies. This quantity is related to the third variation of the total energy, and can be calculated, thanks to an extension of the "2n+1 Wigner's rule", within the DFPT framework. We have developed a practical and efficient method for the calculation of the third derivative of the total energy in a metallic system, within the DFT and DFPT approaches. This method has been explicitly implemented for this work and has made feasible the study within the QHA of systems in which many structural parameters are involved in the thermal expansion.

As far as materials are concerned, in this work we focus our attention on the thermal expansion of Be(0001), Be($10\overline{1}0$), and Mg($10\overline{1}0$) surfaces. Beryllium and Magnesium are particularly indicated to study the QHA, infact, because of the light atomic masses, quantum effects are expected to be more pronounced in determining the low temperature structure, than in other materials. Moreover failure of phenomenological models in describing Be surface dynamical properties [15, 16] make necessary the use of an *ab initio* approach to deal with this metal.

Beryllium (0001) surface has recently attracted much experimental [15, 17, 18] and theoretical [19–22] interest, because of its large outward relaxation. Recently [4] a large thermal expansion of the Be(0001) top layer, has been experimentally observed. The first interlayer spacing expands to 6.7%, with respect to the bulk, at 700 K, and this result was somehow unexpected, however early calculation [4], done within an oversimplified QHA scheme, results in agreement with the experiment. The approximations used in this calculation have been criticized by some authors [5], and this debate has attracted our attention.

In this work we show an *ab initio* study of the thermal expansion of Be(0001) surface [23]. Our results describe very well surface phonon dispersions and the bulk thermal expansion. A very accurate sampling of the vibrational modes, and a careful checking of all the approximations used is done. Furthermore, in order to assess the validity of the QHA we compare our results with first principles MD simulations. In spite of the high accuracy of our calculations, they do not reproduce the large measured thermal expansion, and we argue that the actual surface could be less ideal than assumed.

In the case of Be(0001) surface only one layer is, essentially, involved in the relaxation, and the study of the thermal expansion, within QHA scheme, can be done by direct

numerical derivation of the vibrational frequencies. This approach cannot be used for Be($10\overline{1}0$), and Mg($10\overline{1}0$) surfaces, as these surfaces are more open than the (0001) one, and many layers relax, and are involved in the thermal expansion. As previously mentioned these systems can be studied efficiently by computing analytically third derivatives of the total energy, and are investigated in this work.

A recent experiment for Mg($10\overline{1}0$) surface [24] reports a negative thermal expansion of the first interlayer spacing, (where the surface region is still expanding as a whole), and this is one of the few cases reported so far. Our calculation confirm this result, and predicts the same behaviour also in the case of Be($10\overline{1}0$) surface.

Chapter 1

Motivation of the work

The accurate study of thermal expansion, within a first principles approach, has become nowadays feasible. In this work we are essentially involved in the study of the thermal expansion of metallic surfaces within the QHA, and in this chapter we will show the usefulness of this scheme.

As mentioned in the Introduction one of the main motivations of the present study is to assess the validity of the QHA for the study of surface thermal behaviour, since it has not been widely used so far, and little is known about its accuracy in the surface case. Moreover it has never been used to study systems described by a large number of structural parameters.

In Sec. 1 we review some concepts in lattice dynamics, and in Sec. 2 we compare two possible schemes to deal with thermal expansion: Molecular Dynamics and Quasi Harmonic Approximation. In the remaining of the chapter we discuss some recent experimental results concerning Be and Mg surfaces, that have attracted our attention.

1.1 Lattice dynamics

The study of the motion of a crystal for positions not far from equilibrium can be done within the harmonic approximation [25].

The underlying approximation is the Born-Oppenheimer or adiabatic one. This is a widely used approximation in solid state physics, and consists in decoupling "fast" electronic degrees of freedom from the "slow" ionic ones –by virtue of the great difference of masses– in the Schrödinger equation of interacting electrons and ions. In the adiabatic scheme electrons are considered as quantum particles moving in the potential of the fixed nuclei, and they follows adiabatically the ions, always remaining in their ground state. The ionic motion is then described by an Hamiltonian, whose interatomic potential is the ground state energy of the system of interacting ions and electrons, in which ionic positions are treated as parameters:

$$H = T_{ion} + E(\{\mathbf{R}_{ls}\}), \tag{1.1}$$

where T_{ion} is the kinetic energy of the ions, $E(\{\mathbf{R}_{ls}\})$ is the total energy of the crystal and

R_{ls} is the position of the s_{th} ion in the l_{th} lattice cell. This Hamiltonian can be studied classically or with a quantum mechanical approach.

Since we are studying the system for configuration near the equilibrium we can expand the energy in a Taylor series with respect to the atomic displacements around their equilibrium positions R^0_{ls}:

$$E(\{\mathbf{R}_{ls}\}) = E(\{\mathbf{R}^0_{ls}\}) + \frac{1}{2}\sum_{lsl's'} \left.\frac{\partial^2 E}{\partial \mathbf{u}_s(\mathbf{R}_l)\partial \mathbf{u}_{s'}(\mathbf{R}_{l'})}\right|_0 \mathbf{u}_s(\mathbf{R}_l)\mathbf{u}_{s'}(\mathbf{R}_{l'}) + \mathcal{O}(\mathbf{u}^3), \tag{1.2}$$

where $\mathbf{u}_s(\mathbf{R}_l) = \mathbf{R}_{ls} - \mathbf{R}^0_{ls}$ is the displacement from equilibrium, and the linear term vanishes because of equilibrium. The harmonic approximation consists in truncating this expansion to the second order, thus the classical equations of motion are:

$$M_s \ddot{u}_{\alpha s}(\mathbf{R}_l) = -\frac{\partial E}{\partial u_{\alpha s}(\mathbf{R}_l)} = -\sum_{l's'\beta} C_{\alpha s,\beta s'}(\mathbf{R}_l - \mathbf{R}_{l'}) u_{\beta s'}(\mathbf{R}_{l'}), \tag{1.3}$$

where M_s is the mass of the s_{th} atom, $u_{\alpha s}$ is the α_{th} component in carthesian coordinates of $\mathbf{u}_s$, and:

$$C_{\alpha s,\beta s'}(\mathbf{R}_l - \mathbf{R}_{l'}) = \left.\frac{\partial^2 E}{\partial u_{\alpha s}(\mathbf{R}_l)\partial u_{\beta s'}(\mathbf{R}_{l'})}\right|_0. \tag{1.4}$$

$C_{\alpha s,\beta s'}$ is the interatomic force constant matrix, that depends on $\mathbf{R}_l - \mathbf{R}_{l'}$ because of the translational invariance of the lattice. Other properties are that:

$$C_{\alpha s,\beta s'}(-\mathbf{R}_l) = C_{\beta s',\alpha s}(\mathbf{R}_l), \qquad \sum_{ls s'} C_{\alpha s,\beta s'}(\mathbf{R}_l) = 0 \quad \forall \alpha, \beta \tag{1.5}$$

This second property comes from the invariance of the energy of the system under a continuous translation of the entire crystal without distortion.

Due to translational invariance of the lattice, the solution of the infinite set of coupled Eqs. 1.3 are *normal modes* characterized by a vector $\mathbf{q}$ in reciprocal space and having the form:

$$\mathbf{u}_s(\mathbf{R}_l, t) = \frac{1}{\sqrt{M_s}}\mathbf{v}_s(\mathbf{q}) e^{i\mathbf{q}\mathbf{R}_l - i\omega t}, \tag{1.6}$$

The equations of motions become:

$$\omega^2 v_{\alpha s}(\mathbf{q}) = \sum_{\beta s'} D_{\alpha s,\beta s'}(\mathbf{q}) v_{\beta s'}(\mathbf{q}) \tag{1.7}$$

where $D(\mathbf{q})$ is the *dynamical matrix* defined as:

$$D_{\alpha s,\beta s'}(\mathbf{q}) = \frac{1}{\sqrt{M_s M_{s'}}} \sum_l C_{\alpha s,\beta s'}(\mathbf{R}_l) e^{-i\mathbf{q}\mathbf{R}_l} \tag{1.8}$$

$\mathbf{D}(\mathbf{q})$ is a $3N_{at} \times 3N_{at}$ hermitean matrix –N_{at} is the number of atoms per unit cell– and has the following properties:

$$D_{\alpha s,\beta s'}(\mathbf{q}) = D^*_{\alpha s,\beta s'}(-\mathbf{q}), \qquad D_{\alpha s,\beta s'}(\mathbf{q}) = D^*_{\beta s',\alpha s}(\mathbf{q}). \tag{1.9}$$

Any harmonic vibration of the crystal can be expressed as a linear superposition of normal-mode vibrations, and, given a $\mathbf{q}$ point, eq.1.7 defines the $3N_{at}$ corresponding normal modes and their vibrational frequencies. A complete description of the harmonic properties of a crystal can thus be obtained from the knowledge of the interatomic force constants defined in eqs. 1.4 or 1.8. The quantum mechanical problem, in the harmonic approximation can be solved in a completely analogous way [26].

1.2 Molecular Dynamics and the Quasi Harmonic Approximation

In a purely harmonic crystal, ion mean positions do not change upon increasing temperature, thus crystal thermal expansion is a consequence of anharmonic terms in the interatomic potential. Thermal behaviour of a system can be studied in different ways, and in this work we have used Molecular Dynamic (MD) simulations, and calculations based on the Quasi Harmonic Approximation(QHA).

To perform a MD simulation means to compute the time evolution of a system according to the Newtonian equations of motion. In a free evolution of a sufficiently large system (microcanonical run) the temperature, T, of the system is related to the time average of the kinetic energy by: $\frac{3}{2}K_BT = \langle \frac{1}{2}mv^2 \rangle$. MD simulations account exactly for interatomic potential anharmonicity, but treats ionic degrees of freedom classically, and can give reliable results only near or above Debye temperature, where quantum effects are negligible. Within a first principle approach MD simulations can be a heavy computational task, and as a consequence computationally treatable systems may result not large enough to be physically realistic. Systems that can be simulated, nowadays, typically consist of about a hundred atoms and the time scale of the simulation can reach a few picoseconds.

The QHA provides a complementary approach, valid below the melting temperature to determine the temperature dependence of structural properties. In this approximation, the equilibrium structural parameters, $\mathbf{a} = (a_1, a_2, a_3, \ldots)$, of a crystal, at any fixed temperature T, are obtained by minimizing the Helmholtz free energy F of a system of purely harmonic oscillators having the frequencies of the vibrational modes of the crystal $\omega_{\nu\mathbf{q}}(\mathbf{a})$ in that configuration:

$$F(T,\mathbf{a}) = E^{tot}(\mathbf{a}) + F^{vib}(T,\mathbf{a}) =$$

$$= E^{tot}(\mathbf{a}) + \sum_{\nu,\mathbf{q}} \left\{ \frac{\hbar\omega_{\nu\mathbf{q}}(\mathbf{a})}{2k_BT} + k_BT \ln\left(1 - e^{-\frac{\hbar\omega_{\nu\mathbf{q}}(\mathbf{a})}{2k_BT}}\right) \right\}, \tag{1.10}$$

$$\frac{\partial F(T,\mathbf{a})}{\partial \mathbf{a}} = 0, \tag{1.11}$$

where $E^{tot}(\mathbf{a})$ is the static energy of the crystal. To apply this model, the knowledge of $\omega_{\nu\mathbf{q}}(\mathbf{a})$ as a function of the structural parameters is requested, thus including some anharmonic effects.

Application of the QHA scheme is difficult, from a computational point of view, because of the calculation of F^{vib}. One must be able to calculate frequencies all over the

Brillouin Zone, and this can be done exactly using DFPT [10, 11]. Furthermore this calculation must be performed at various values of the structural parameters.

As an example, in the simple case of anisotropic thermal expansion of an *hcp* crystal (the system is described by two parameters that are the length of the two axis a and c) one can compute phonon dispersions in a grid of points in the (a, c) space and interpolate in between the second term of eq. 1.10. On the other hand if the system is described by a large number of structural parameters (we will show that this is the case for *hcp*$(10\overline{1}0)$ surfaces) the Free energy cannot be directly calculated varying every parameter involved in the expansion.

In the general case one can proceed being able to compute the vibrational forces $\frac{\partial F^{vib}}{\partial a_i}$. As a first approximation, assuming a linear dependence of F^{vib} on its arguments, eq. 1.11 becomes:

$$\frac{\partial F^{vib}}{\partial a_i} + \frac{\partial E^{tot}}{\partial a_i}(\mathbf{a}) = 0. \tag{1.12}$$

Within a first principles approach $\frac{\partial E^{tot}}{\partial a_i}(\mathbf{a})$ can be calculated in every point of the space $\mathbf{a}$ thanks to the Hellmann Feynmann theorem [27], thus eq. 1.12 can be easily solved. Once obtained in this way an estimate of the equilibrium parameters of the system, an exact solution to the problem could in principle be obtained by calculating vibrational forces in the new point and iterating the procedure to self consistency.

Using a slightly different notation eq. 1.7 can be rewritten:

$$\omega^2_{\nu\mathbf{q}}\mathbf{v}_{\nu\mathbf{q}} = \mathbf{D}(\mathbf{q})\mathbf{v}_{\nu\mathbf{q}}, \tag{1.13}$$

with this notation the derivative of the vibrational free energy is given by:

$$\frac{dF^{vib}}{da_i} = \frac{\hbar}{4}\sum_{\nu,\mathbf{q}}\frac{1}{\omega_{\nu\mathbf{q}}} tgh^{-1}\left(\frac{\hbar\omega_{\nu\mathbf{q}}}{2k_BT}\right)\frac{\langle\mathbf{v}_{\nu\mathbf{q}}|\frac{d}{da_i}\mathbf{D}(\mathbf{q})|\mathbf{v}_{\nu\mathbf{q}}\rangle}{\sum_{\alpha,s}|\mathbf{v}_{\alpha,s}|^2 m_s}. \tag{1.14}$$

Since the dynamical matrix $\mathbf{D}(\mathbf{q})$ is the second derivative of the total energy with respect to atomic displacements, to calculate the derivative of F^{vib} with respect to atomic displacements the calculation of the third derivatives of the total energy is necessary.

1.3 Beryllium vs. Magnesium

Be and Mg are simple metals with the same outermost electronic configuration but different properties. They are respectively the 2^{nd} and the 3^{rd} element in the 2^{nd} column of the periodic table. In both cases the outermost electronic configuration of the isolated atom consists of a filled s-shell (Be:$2s^2$, Mg:$3s^2$) and so, in order to form a bond, outermost electrons must hybridize with p states. At room temperature and atmospheric pressure Be and Mg are stable in the hexagonal close packed (*hcp*) crystalline structure (Fig. 1.1). A more pronounced covalent character of the bonding in Be reflects in some physical properties that make Be different from Mg and from the other elements of the same column.

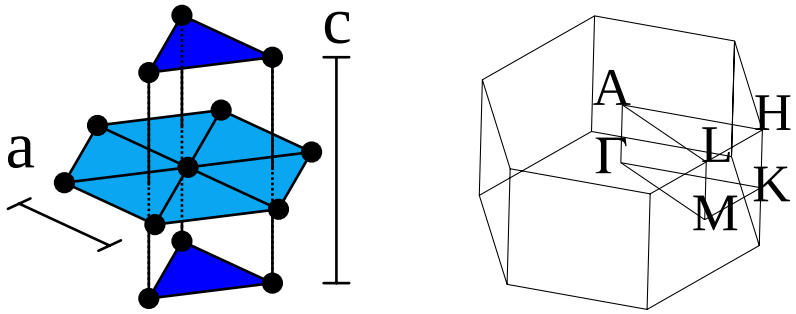

Figure 1.1: Schematic drawing of the hcp crystal structure, and of the corresponding Brillouin zone.

The bonding energy of Be is surprisingly strong when compared with close neighbors in the Periodic Table (cohesive energy Be: 3.32 eV/atom, Mg: 1.51 eV/atom, Li: 1.63 eV/atom [28]). Also the Debye temperature is very high (Be: 1440 K, Mg: 400 K, Li: 344 K [29]), and thus quantum effects should be more pronounced in determining zero temperature structural properties.

There are some evidence of directional bonding in Be. First of all Be c/a ratio is one of the most contracted ($\simeq 4\%$) for *hcp* metals, unlike the nearly ideal one of Mg (ideal c/a $\simeq$1.63, Mg: 1.62, Be: 1.57), thus out-of-plane neighbours have shorter bonds than in-plane neighbours. Another evidence of this anisotropy is that the contribution to the density of electronic states coming from p_x and p_y states is different from the one from p_z [30].

Beryllium density of electronic states resembles somewhat that one of a semiconductor, since it has a minimum near the Fermi energy, while the one of Mg is nearly free electron like ($\simeq \sqrt{\epsilon}$) as shown in Fig. 1.2. In Fig. 1.2 the comparison between calculated Be and Mg electronic dispersion is also shown . Note that Beryllium bands display a direct gap in a large part of the shown BZ, unlike Mg. Mg has a filled state at Γ with energy $\simeq -1.3eV$, while the corresponding Be state is above the Fermi energy and its band is nearly flat. This band is the source of both the low density of states near the Fermi energy and the high peak above the Fermi energy.

The vibrational motion of atoms in a crystal is related to the direct ion-ion interaction and to the screening properties of the electronic distribution which can give rise to non-central forces between ions. For many non-transition metals lattice dynamics can be correctly described in terms of pairwise central forces, and this can be done, approximatively, for bulk Mg [31]. On the contrary without taking into account non-central forces it is impossible to describe even qualitatively Be bulk phonon dispersion [31–33]. For instance by group theoretical analysis it can be shown, quite generally, that at K$= (0, 2/3, 0)2\pi/a$, in an hcp crystal, there are three vibrational modes polarized in the basal plane. One of the modes is doubly degenarate, the other two are non degenerate. If the dynamical properties depend only on pairwise central forces the frequency of the degenerate mode lies in between the other two. This ordering of the frequencies is incompatible with the

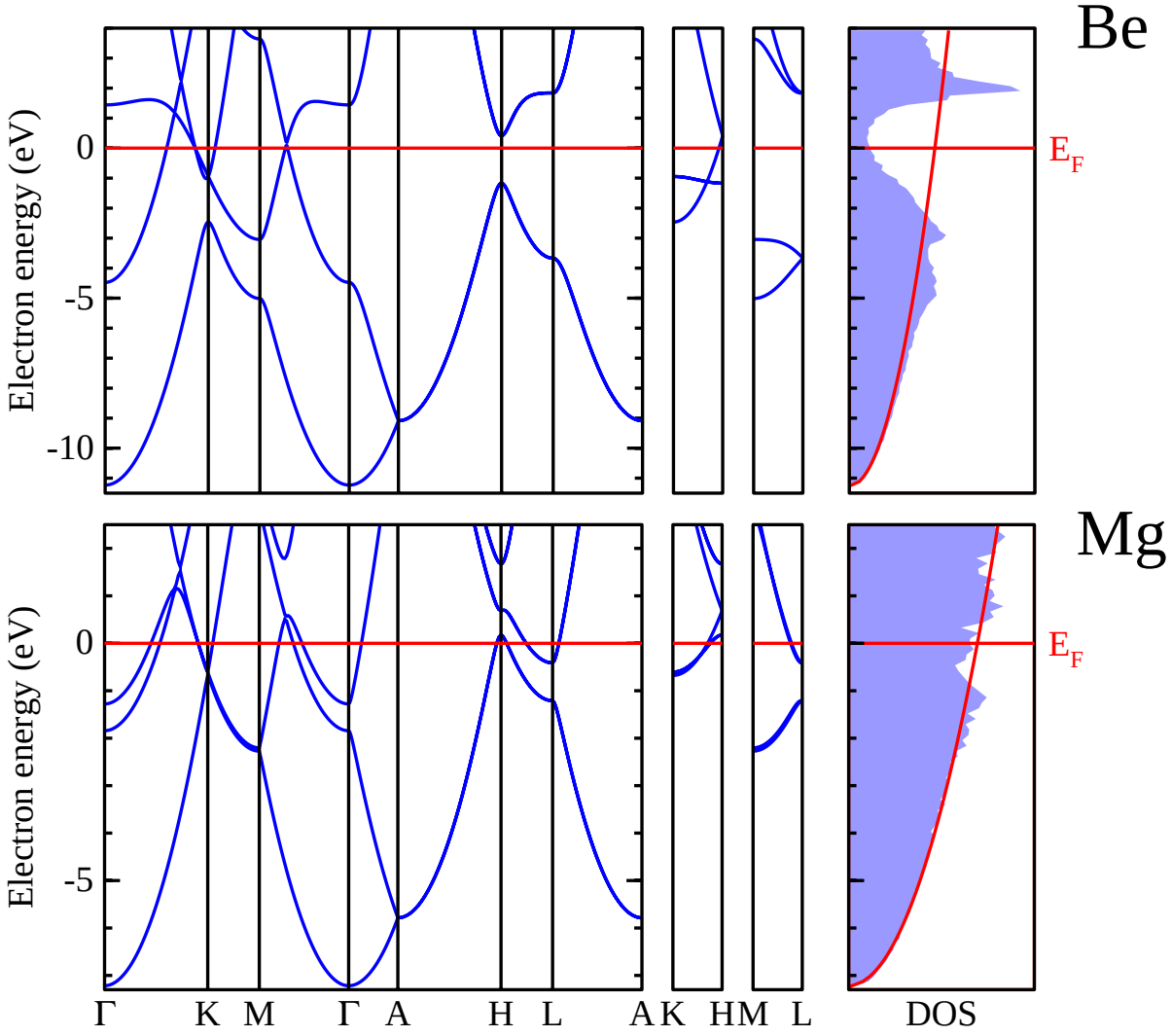

Figure 1.2: Comparison between Be and Mg electronic band structure calculated by first-principle methods. Density of States(DOS) is also shown. In the DOS panel the free electron like DOS of the corresponding material is also shown. Be and Mg have the same outermost electronic configuration, but while Mg DOS is nearly free electron like, Be DOS "resembles" that one of a semiconductor, having a minimum near the Fermi energy.

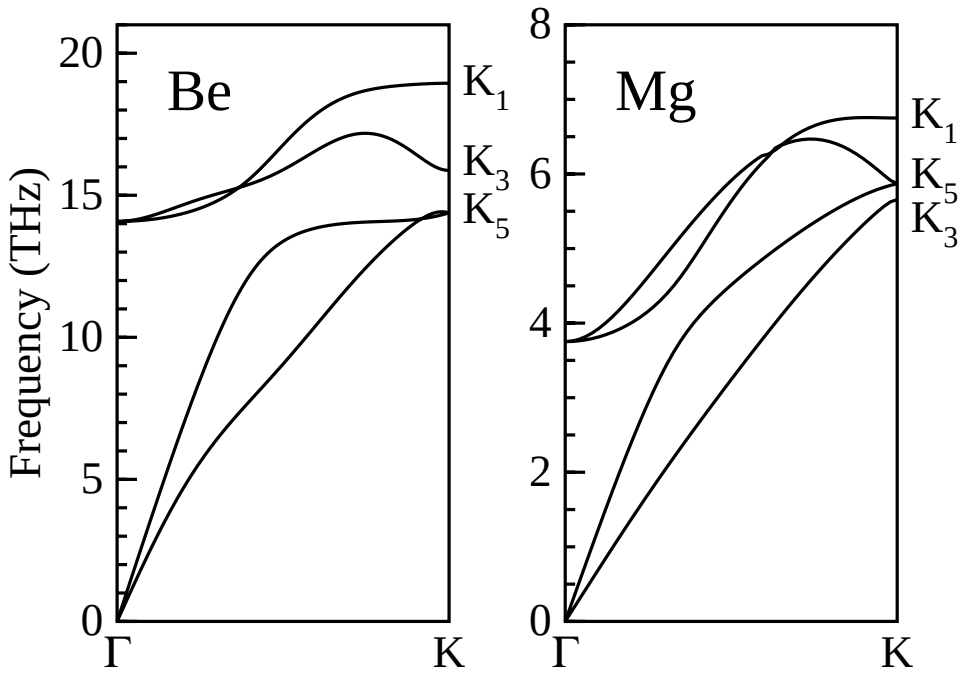

Figure 1.3: Accurate calculation of Beryllium and Magnesium bulk phonon dispersions of the three modes polarized in the basal plane in the Γ-K direction. The ordering of the three modes at K for Be, is incompatible with a pairwise central force model (see text).

one found in Be, unlike Mg (Fig. 1.3).

1.4 Be(0001) surface

Because of its large outward relaxation [17] Beryllium (0001) surface has attracted much experimental [15, 17, 18] and theoretical [19–22] interest. It is a close-packed surface, similar to the (111) surface of an fcc crystal. It is well established that the first interlayer separation on most metal surfaces is contracted at room temperature, Be(0001) is one of the few exceptions reported so far.

Until very recently there was a substantial disagreement between experimental and first-principles theoretical [19, 21, 22] results on the amount of topmost interlayer expansion in this system, theoretical calculations giving roughly half of the observed value. In a recent letter, Pohl and coworkers [4] reconcile experiment and theory on this point showing that low temperature (110 K) low-energy electron diffraction (LEED) determinations of the first interlayer separation ($d_{12} \simeq +3.3\%$ at T=110K) are in agreement with first-principles calculations and that reported discrepancies at room temperature originate from a large thermal expansion of the top layer, reaching 6.7% at 700 K. These findings are very interesting and puzzling, since surface phonons show no sign of enhanced anharmonicity [4, 15], however the calculation of the surface thermal expansion [4], within a simplified quasiharmonic approach recently introduced in Ref. [6, 34], results in very good agreement with experiments.

Table 1.1: Mg($10\bar{1}0$) surface: LEED-IV measurements[24] of the two outer layers thermal expansion.

	$d_{12}(\%)$	$d_{23}(\%)$
T=120 K	-16.4	+7.8
T=300 K	-20.1	+9.4
T=400 K	-20.6	+10.6

As mentioned previously, within the quasi-harmonic approximation the determination of $d_{12}(T)$ can be done by minimizing the free energy of the system (eq. 1.10), with respect to d_{12}. Since the evaluation of the free energy requires the knowledge of the phonon spectrum all over the Brillouin zone, that is a heavy computational task, some simplifications have been introduced in Ref. [6, 34] . In particular only three modes at the zone center are calculated and the frequency so obtained are used to sample the vibrational density of states in the free energy calculation. The validity of such an approach has been criticized by some authors [5], because of the very poor sampling of vibrational modes adopted.

In Chap. 4 we address this surface by performing full BZ sampling and comparing our result with first principles MD simulations. Careful checking of all the approximation used will also be shown.

1.5 Mg($10\bar{1}0$) surface

A schematic drawing of the ($10\bar{1}0$) surface is reported in Fig. 1.4. This surface is more open than the(0001) one, and in principle, the truncated bulk can be terminated in two ways, either with a short first interlayer separation, d_{12}, as shown in Fig. 1.4, or with a long one, (that can be obtained removing the top-layer from the short-terminated surface).

Recently LEED measurements have determined the termination and interplanar separation of the clean Mg ($10\bar{1}0$) surface as a function of temperature [24]. The preferred termination is the one with short d_{12} and many layers are involved in the relaxation in an oscillatory way: while the first interlayer contracts the second expands and so on. Measurement (Tab. 1.1) indicates a negative thermal expansion of the first interlayer spacing, and these results have not been confirmed by theory, yet.

In Chap. 4 we report on our study, within QHA approach, of the thermal behaviour of this surface. This kind of study has been possible thanks to the development of a method to calculate third order derivative of the total energy in a metallic system.

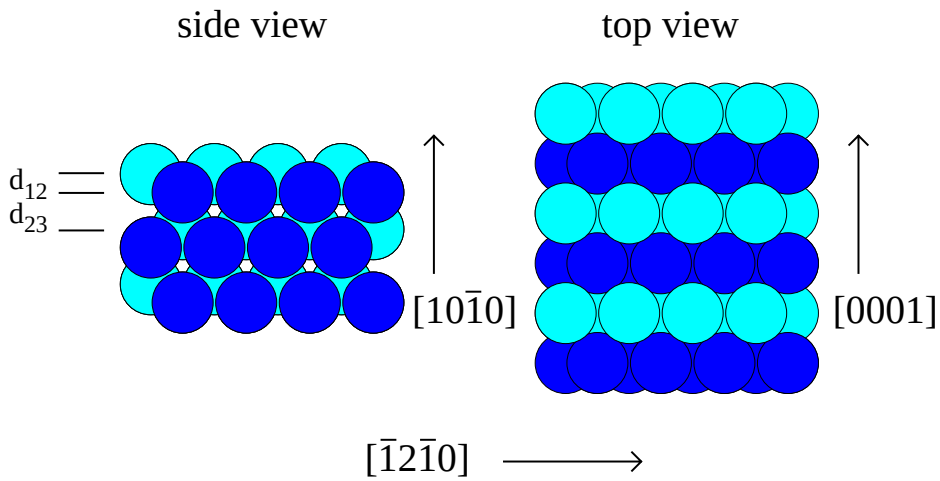

Figure 1.4: Schematic drawing of the (10$\bar{1}$0) surface of an *hcp* crystal. The truncated bulk can be terminated in two ways, either with a short first interlayer separation d_{12}, or with a long one. Here only the termination with the shortest d_{12} is plotted, the long-termination can be obtained removing the top-layer from the short terminated surface. Both in Be and in Mg the short termination has been theoretically shown to be the most stable and the one observed in the experiments [24, 35].

Chapter 2

First principles methods

In the previous chapter (Sec. 1.1 and 1.2) we have shown that a complete study of dynamical properties and of thermal expansion, within the quasi-harmonic approximation, can be performed knowing the second and third derivatives of the total energy of a system with respect to atomic displacements.

In this chapter we give an overview of the theoretical tools used in this work to calculate crystal energy and its derivatives up to third order. We have used *ab initio* methods based on Density Functional Theory (DFT)[7, 8]. These methods have been developed in the last 30 years and have demonstrated to be one of the most powerful tool in the theory of the electronic properties of solids, with results and accuracy surprising and unexpected [36–38].

In order to calculate the ground state energy of a quantum mechanical system, in principle, it is not necessary to solve directly Schrödinger equation, and to know the ground state wave function. Within the DFT scheme the basic quantity to be calculated is the electronic charge density, and in principle the second and third order derivatives of the ground state energy can be obtained from the knowledge of the first variation of the electronic charge density thanks to an extension of the "$2n + 1$" theorem [39].

Once the unperturbed problem has been solved in the framework of DFT, Density Functional Perturbation Theory (DFPT) [10, 11] provides an efficient method to calculate the electronic linear response to an external perturbation of arbitrary wavelength. DFPT has been successfully applied to predict vibrational properties of elemental and binary semiconductors [11] or insulators [40], heterostructures [41], semiconductor alloys [42, 43] and surfaces [44], furthermore it has allowed calculation of phonon dispersions in metallic bulk [45] and surfaces [46]. DFPT has already allowed third order calculation in semiconducting systems [47], and in this chapter we will show an extension of this scheme to metals.

In Sec. 1 we give an account of the quite standard *ab initio* methods used in this work to calculate total energy. In Sec. 2, and Sec. 3, after an overview of DFPT we show how vibrational properties can be calculated in this framework. Finally in Sec. 4 we will develop a practical and efficient method for the calculation of the third derivative of the total energy for metallic systems.

2.1 The electronic problem

The Born-Oppenheimer, or adiabatic, approximation, already addressed in Sec. 1.1, reduce the full electronic + ionic problem to the calculation of the electronic ground state energy in the potential energy determined by fixed ions.

2.1.1 Density Functional Theory

The theoretical framework of first-principles calculation used in this work is given by Density Functional Theory, which has become one of the most powerful tools in the theory of the electronic properties [36–38]. W. Kohn is one of the developer of DFT and essentially gave a rigorous theoretical background to it [7, 8]. For this he has been awarded with the 1998 Nobel Prize for Chemistry.

Given a many-body Hamiltonian of interacting electrons in an external potential $v(\mathbf{r})$,– that in our case is generated by ionic cores– one can solve, in principle, the Schrödinger equation and obtain the ground state many-body wavefunction $|\psi_G\rangle$, the ground state energy E_G, and the electronic density $n(\mathbf{r})$.

Hohemberg-Kohn theorem [7] states that, for a given $n(\mathbf{r})$, the $v(\mathbf{r})$ generating it is unique. According to this theorem we can define $F[n(\mathbf{r})]$ as a universal (in the sense that it does not depend on $v(\mathbf{r})$) functional of $n(\mathbf{r})$:

$$F[n(\mathbf{r})] = \langle\psi_G|H_0|\psi_G\rangle = E_G[n(\mathbf{r})] - \int v(\mathbf{r})n(\mathbf{r})d\mathbf{r} \tag{2.1}$$

where H_0 is the Hamiltonian of the interacting electrons, without the external potential.

For fixed external potential, $v(\mathbf{r})$, we can define the energy functional as:

$$E_v[n(\mathbf{r})] = F[n(\mathbf{r})] + \int v(\mathbf{r})n(\mathbf{r})d\mathbf{r}. \tag{2.2}$$

Hohemberg and Kohn also demonstrate [7] that if $n(\mathbf{r})$ is allowed to vary over a range of functions satisfying the requirement

$$N = \int n(\mathbf{r})d\mathbf{r} \tag{2.3}$$

in correspondence of the ground-state electron density the following stationary principle is valid:

$$\delta E_v[n] = 0. \tag{2.4}$$

It follows from this theorem that without solving the Schrödinger equation –and so without calculating the wavefunction of a many-body system– one can, in principle, calculate the ground state energy and the charge density of a system. This could be done exactly if the form of the functional 2.1 were known.

Application of this variational principle allows to deduce very simple one-particle equations, known as Kohn and Sham equations [8]. In order to derive them it is customary to separate $F[n(\mathbf{r})]$ in the following way:

$$F[n(\mathbf{r})] = T_0[n(\mathbf{r})] + \frac{1}{2}\int \frac{n(\mathbf{r})n(\mathbf{r}')}{|\mathbf{r}-\mathbf{r}'|}d\mathbf{r}d\mathbf{r}' + E_{xc}[n(\mathbf{r})] \tag{2.5}$$

where $T_0[n(\mathbf{r})]$ is defined as the kinetic energy of a system of non interacting electrons having $n(\mathbf{r})$ as the ground state density. The two following terms are commonly called Hartree term (E_H), and exchange-correlation energy functional. Eq. 2.5 is the definition of E_{xc} in terms of the unknown functional $F[n]$ and of two well defined quantities, $T_0[n]$, and $E_H[n]$.

With this definition, the set of KS equations is the following and is to be solved self-consistently:

$$\left[\frac{p^2}{2m} + V^{KS}(\mathbf{r})\right]\psi_i(\mathbf{r}) = \epsilon_i\psi_i(\mathbf{r}) \tag{2.6}$$

$$V^{KS}(\mathbf{r}) = \int \frac{n(\mathbf{r}')}{|\mathbf{r}-\mathbf{r}'|}d\mathbf{r}' + \frac{\delta E_{xc}[n]}{\delta n(\mathbf{r})} + v(\mathbf{r}) \tag{2.7}$$

$$n(\mathbf{r}) = \sum_{i=1}^{N} |\psi_i(\mathbf{r})|^2 \tag{2.8}$$

Thus in DFT the calculation of the ground-state properties is reduced to a problem of noninteracting electrons in an effective potential. The ground state energy of the system is given by:

$$E_v[n] = E_I[n] + \sum_{i=1}^{N}\langle\psi_i|\frac{p^2}{2m}|\psi_i\rangle =$$

$$= \sum_{i=1}^{N}\epsilon_i + \left\{E_I[n] - \int V^{KS}(\mathbf{r})n(\mathbf{r})d\mathbf{r}\right\}, \tag{2.9}$$

where

$$E_I[n] = \frac{1}{2}\int \frac{n(\mathbf{r})n(\mathbf{r}')}{|\mathbf{r}-\mathbf{r}'|}d\mathbf{r}d\mathbf{r}' + E_{xc}[n] + \int v(\mathbf{r})n(\mathbf{r})d\mathbf{r}. \tag{2.10}$$

2.1.2 Local Density Approximation

To implement Eq. 2.6 in practice an explicit expression for E_{xc} is needed, and in this work we have used the Local Density Approximation (LDA):

$$E_{xc}^{LDA}[n(\mathbf{r})] = \int n(\mathbf{r})\epsilon_{xc}^{hom}(n(\mathbf{r}))\ d\mathbf{r}, \tag{2.11}$$

where $\epsilon_{xc}^{hom}(n)$ is the exchange and correlation energy per particle of a uniform electron gas of density n. It is a very natural approximation for a system with slowly varying density and it works surprisingly well for a large variety of systems, even better than any early expectations. In the last decade, many improvements to LDA were proposed [48–50], including inhomogeneity corrections via density gradient expansions of various kinds, however none of them seems to provide a definite improvement in all cases.

2.1.3 Plane Waves and Pseudo Potential approach

The actual solution of KS equations can be obtained expanding the KS wavefunctions on a finite basis set. One of the most widely used choices for this basis set is that of plane waves (PW). From the Bloch theorem it comes out that:

$$\psi_{\nu,\mathbf{k}}(\mathbf{r}) = \sum_{\mathbf{G}} e^{i(\mathbf{k}+\mathbf{G})\mathbf{r}} c_\nu(\mathbf{k}+\mathbf{G}) \tag{2.12}$$

where $\mathbf{k}$ belongs to the first Brillouin Zone (BZ) of the crystal, $\mathbf{G}$ is a reciprocal lattice vector and ν is the band index. The PW basis set is infinite and it is usually truncated by choosing a kinetic energy cutoff through the condition:

$$|\mathbf{k}+\mathbf{G}|^2 \leq E_{cut}. \tag{2.13}$$

To treat explicitly all the electrons it would be necessary to choose a very large number of PW in order to describe accurately their rapid oscillations near the nuclei. This problem can be avoided freezing the core electrons in the atomic configuration around the ions, and considering only the valence electrons. To this end one introduces *pseudopotentials* able to describe the interactions between valence electrons and the *pseudoions* (ions+ core electrons). The resulting valence electrons wavefunctions are considerably smoother near the nucleus, but are identical to the "true" wavefunctions outside the core region. This method is now well-established in computational physics, and its results are very accurate [51–55].

The widely-used norm-conserving pseudopotentials act in different ways on the different angular momentum components, l, of the wavefunction, and, for each angular momentum, usually consist of a local contribution for the radial function and a non-local one for the angular part:

$$v_s(\mathbf{r},\mathbf{r}') = v_s^{loc}(r)\delta(\mathbf{r}-\mathbf{r}') + \sum_{l=0}^{l_{max}} v_{s,l}(r)\delta(r-r')P_l(\hat{\mathbf{r}},\hat{\mathbf{r}}'), \tag{2.14}$$

where P_l is the projector on the angular momentum l. This form of *semilocal* pseudopotential is still not the most convenient one from a computational point of view, and for this reason Kleinman and Bylander (KB) introduced [56] a fully non-local pseudopotential in which also the radial part of the potential is non-local:

$$v_s^{(NL)}(\mathbf{r},\mathbf{r}') = v_s^{loc}(r)\delta(\mathbf{r}-\mathbf{r}') + \sum_{l=0}^{l_{max}} v_{s,l}^{(NL)}(\mathbf{r},\mathbf{r}'), \tag{2.15}$$

where

$$v_{s,l}^{(NL)}(\mathbf{r},\mathbf{r}') = \sum_{m=-l}^{l} \frac{v_{s,l}(r)R_{s,l}(r)Y_l^m(\theta,\phi)Y_l^{*m}(\theta',\phi')R_{s,l}(r')v_{s,l}(r')}{\langle R_{s,l}|v_{s,l}|R_{s,l}\rangle}. \tag{2.16}$$

This form of the potential allows a very convenient simplification of its matrix elements in reciprocal space, where the KS equations are iteratively solved.

2.1.4 Smearing technique

Calculation of many quantities for crystalline solids involves integration over **k** vectors of Bloch functions in the Brillouin zone. These integration are commonly approximated by summation over a finite set of sampling **k** points, weighted with the occupation number of the electronic states:

$$F = \frac{\Omega}{(2\pi)^3} \int_{BZ} \theta(\epsilon_F - \epsilon_\nu(\mathbf{k})) f(\mathbf{k}) d\mathbf{k} \simeq \sum_{i=1}^{N} \theta(\epsilon_F - \epsilon_\nu(\mathbf{k}_i)) f(\mathbf{k}_i) \tag{2.17}$$

where $\epsilon_\nu(\mathbf{k})$ is the energy of an electronic state, ϵ_F is the Fermi energy and $\theta(x)$ is the step function: $x < 0 \Rightarrow \theta(x) = 0$, and $x > 0 \Rightarrow \theta(x) = 1$. In the case of metals, due to the presence of energy bands that cross the Fermi energy, the integrand is discontinuous and a large number of points must be used to reach sufficient accuracy.

The smearing approach consists in using a continuous smeared function $\tilde{\theta}(x)$, characterized by a smearing width σ, instead of the step function $\theta(x)$. Smoothing the integrand the calculation converges better, but the results are obviously affected. The only justification for this *ad hoc* procedure is that in the limit as $\sigma \to 0$ one would recover the "absolutely" converged result (at the expense of using a prohibitively fine **k** mesh), and that even at finite value of σ one can obtain accurate results. Many kind of smearing functions can be used: Fermi-Dirac broadening, Lorentzian, Gaussian [57], or Gaussian combined with polynomials [58], to recall only some of them.

Within this approach we should substitute, in the Kohn-Sham equations, eq. 2.8 with:

$$n(\mathbf{r}) = \sum_i \tilde{\theta}(\epsilon_F - \epsilon_i) |\psi_i(\mathbf{r})|^2, \tag{2.18}$$

$$\int n(\mathbf{r}) d\mathbf{r} = N = \sum_i \tilde{\theta}(\epsilon_F - \epsilon_i) \tag{2.19}$$

where the Fermi energy ϵ_F is defined by eq. 2.19. The natural definition of the total energy of the system becomes:

$$E_v[n] = \int_{-\infty}^{\epsilon_F} \epsilon n(\epsilon) d\epsilon + \left\{ E_I[n] - \int \frac{\delta E_I[n]}{\delta n(\mathbf{r})} n(\mathbf{r}) d\mathbf{r} \right\} =$$

$$= \sum_i \{ \tilde{\theta}_1(\epsilon_F - \epsilon_i) + \epsilon_i \tilde{\theta}(\epsilon_F - \epsilon_i) \} + \left\{ E_I[n] - \int \frac{\delta E_I[n]}{\delta n(\mathbf{r})} n(\mathbf{r}) d\mathbf{r} \right\} \tag{2.20}$$

where $\tilde{\theta}_1(x) = \int_{-\infty}^{x} y\tilde{\delta}(y) dy$, and $\tilde{\delta}(x) = \frac{\partial}{\partial x}\tilde{\theta}$. It can be shown that the new K-S equations come out from the minimization of this total energy.

2.1.5 Non Linear Core Correction

In their simple original form, norm-conserving pseudopotentials substitute the valence-only charge density to the total one in all contributions to the total energy. While this is correct, within the frozen core approximation, for the Hartree term, this is only approximate for exchange-correlation contribution, due to its non-linear form. The idea

underlying the Non Linear Core Correction (NLCC) is to use the *total* charge instead of the *valence* charge to compute the exchange-correlation energy [59]:

$$E_{xc} = \int_V (n_v(\mathbf{r}) + n_c(\mathbf{r}))\epsilon_{xc}(n_v(\mathbf{r}) + n_c(\mathbf{r}))d\mathbf{r}, \tag{2.21}$$

where n_c is the charge density of the core electrons, computed as a superposition of the atomic core charges of the atoms which require NLCC, and n_v is the valence charge. The core charge is computed only once, together with the psuedopotential and then it is added to the valence charge to compute the exchange-correlation energy.

This correction is particularly important when there is a significant overlap between valence and core charge, as in the case of Beryllium and Magnesium atoms, and improves the transferability of the corresponding pseudopotentials.

2.2 Density Functional Perturbation Theory

Once the unperturbed problem has been solved in the framework of DFT, DFPT [10, 11] provides an efficient method to calculate the electronic linear response to an external perturbation of arbitrary wavelength. DFPT has been developed for semiconductors and successively adapted to metallic systems [45]. We will state DFPT for metals in a way slightly different and less elegant than in [45], because in the present form it is more appropriate to the purpose of this work.

When a perturbation $V^{(1)}_{bare}$ is superimposed on the external potential acting on a KS system, the self consistent potential is modified accordingly: $V_{SCF} \to V_{SCF} + V^{(1)}_{SCF}$. If $V^{(1)}_{SCF}$ is assumed to be known, from standard first order perturbation theory the linear variation of a wavefunction $\psi^{(1)}$ and thus the linear variation of electron density $n^{(1)}$ can be calculated. The response to a particular external perturbation can be obtained by iteration up to self-consistency. The system of equations to be solved in the semiconductor case is the following:

$$[H_{KS} + \alpha P_v - \epsilon_i]|P_c\psi^{(1)}_i\rangle = -P_c V^{(1)}_{SCF}|\psi_i\rangle \tag{2.22}$$

$$n^{(1)} = \sum_i \{|\psi_i\rangle\langle P_c\psi^{(1)}_i| + cc.\} \tag{2.23}$$

$$V^{(1)}_{SCF}(\mathbf{r}) = V^{(1)}_{bare}(\mathbf{r}) + \int \frac{n^{(1)}(\mathbf{r}')}{|\mathbf{r} - \mathbf{r}'|}d\mathbf{r}' + \left.\frac{dv_{xc}}{dn}\right|_{n=n_0(\mathbf{n})} n^{(1)}(\mathbf{r}) \tag{2.24}$$

where i runs over the occupied states, P_c and P_v are projectors on conduction and valence states, and α is an energy chosen so as eq. 2.22 not to be singular. Note that, in order to solve this system, the knowledge only of the unperturbed valence ground states is required, and thus the calculation can be implemented efficiently.

To extend this approach to a metallic system, one can consider an energy sufficiently high, in order to separate partially occupied states from empty ones. Chosen an energy $\bar{E} > \epsilon_F + 3\sigma$, where σ is the width of the smearing function $\tilde{\theta}$, eq. 2.22, and 2.23 become:

$$[H_{KS} + \alpha P_{\bar{v}} - \epsilon_i]|P_{\bar{c}}\psi^{(1)}_i\rangle = -P_{\bar{c}} V^{(1)}_{SCF}|\psi_i\rangle \tag{2.25}$$

$$n^{(1)} = \sum_i \tilde{\theta}_{Fi}\{|P_{\bar{c}}\psi_i^{(1)}\rangle\langle\psi_i| + cc\}+$$

$$\sum_{ij}^{\bar{v}} \frac{\tilde{\theta}_{Fi} - \tilde{\theta}_{Fj}}{\epsilon_i - \epsilon_j}|\psi_j\rangle\langle\psi_j|V_{SCF}^{(1)}|\psi_i\rangle\langle\psi_i| + \sum_i \tilde{\delta}_{Fi}\epsilon_F^{(1)}|\psi_i\rangle\langle\psi_i| \tag{2.26}$$

where $P_{\bar{v}}$ ($P_{\bar{c}}$) is a projector on band states with energy $\leq \bar{E}(> \bar{E})$, $\sum^{\bar{v}}$ is a summation on states with energy $\leq \bar{E}$, $\tilde{\theta}_{Fi} = \tilde{\theta}(\epsilon_F - \epsilon_i)$, and $\tilde{\delta}_{Fi} = \frac{\partial}{\partial x}\tilde{\theta}(x)\Big|_{\epsilon_F - \epsilon_i}$. Eq. 2.25 should be solved only for occupied states, and α is to be chosen so as eq. 2.25 not to be singular. Also in this case the solution of the system requires the knowledge of only a finite number of states of the unperturbed K-S Hamiltonian –those with energy $< \bar{E}$–.

2.3 Second order and Linear response

The electronic linear response to ionic displacements considered as external perturbations gives access to interatomic force constants. Infact, within the adiabatic approximation, a lattice vibration can be seen as a static perturbation acting on electrons, and the linear variation of electron density upon application of an external perturbation determines energy variation up to third order [60].

Given a Kohn-Sham system in which the bare external potential acting on electrons $V_{\boldsymbol{\lambda}}^{ion}$is a function of some parameters $\boldsymbol{\lambda}$, the Hellmann-Feynmann theorem [27] states that:

$$\frac{\partial E_{\boldsymbol{\lambda}}^{el}}{\partial \lambda_i} = \int n_{\boldsymbol{\lambda}}(\mathbf{r})\frac{\partial V_{\boldsymbol{\lambda}}^{ion}}{\partial \lambda_i}(\mathbf{r})d\mathbf{r}, \tag{2.27}$$

where $E_{\boldsymbol{\lambda}}^{el}$ is the electronic ground-state energy relative to some given values of the parameters $\boldsymbol{\lambda}$, and $n_{\boldsymbol{\lambda}}$ is the corresponding electron density distribution. Differentiating this expression one obtains:

$$\left.\frac{\partial^2 E_{\boldsymbol{\lambda}}^{el}}{\partial\lambda_i\partial\lambda_j}\right|_0 = \int \left[\left.\frac{\partial n_{\boldsymbol{\lambda}}(\mathbf{r})}{\partial\lambda_j}\right|_0 \left.\frac{\partial V_{\boldsymbol{\lambda}}^{ion}(\mathbf{r})}{\partial\lambda_i}\right|_0 + n_0(\mathbf{r})\left.\frac{\partial^2 V_{\boldsymbol{\lambda}}^{ion}(\mathbf{r})}{\partial\lambda_i\partial\lambda_j}\right|_0\right] d\mathbf{r}. \tag{2.28}$$

From this equation it results that from the knowledge of the linear response of the electronic charge, the second derivative of the total energy, and thus the dynamical matrix, can be calculated as:

$$D_{\alpha s,\beta s'}(\mathbf{q}) = D_{\alpha s,\beta s'}^{el}(\mathbf{q}) + D_{\alpha s,\beta s'}^{ion}(\mathbf{q})$$

$$D_{\alpha s,\beta s'}^{el}(\mathbf{q}) = \int \left(\frac{\partial n(\mathbf{r})}{\partial u_{\alpha s}(\mathbf{q})}\right)^* \frac{\partial V^{ion}(\mathbf{r})}{\partial u_{\beta s'}(\mathbf{q})}d\mathbf{r} + \delta_{ss'}\int n_0(\mathbf{r})\frac{\partial^2 V^{ion}(\mathbf{r})}{\partial u_{\alpha s}(\mathbf{q}=0)u_{\beta s}(\mathbf{q}=0)}d\mathbf{r}. \tag{2.29}$$

There are two contributions: one is due to the electronic charge variation, while the second comes from the direct electrostatic interaction between ions, and is essentially the second derivative of an Ewald sum [61]. DFPT permits to calculate linear response to perturbation having an arbitrary wavelength $\mathbf{q}$, and so every term in eq. 2.29 can be calculated within this framework.

2.4 Third order for metals

In this section we develop a method to calculate the third order derivative of the total energy for a metallic system. This method allows the calculation of the derivatives of the dynamical matrix that will be used to study thermal expansion within the Quasi Harmonic Approximation [25].

In ordinary quantum mechanics Rayleigh-Schrödinger perturbation theory there exist a well known result, called Wigner's $2n+1$ rule [39], which yields energy derivatives through order $2n+1$ starting from the knowledge of the $n-th$ derivative of wavefunctions. This rule comes from a general principle [62] and its applicability to self consistent field theories has been known since several years [63, 64]. '2n+1' rule has been generalized to DFT by Gonze and Vigneron [60], and has already been applied to semiconducting systems [47] but not yet to metallic systems.

In what follows we will indicate the $n-th$ derivative of a quantity F, with respect to a parameter λ, equivalently by $F^{(n)}$ or $\frac{d^n}{d\lambda^n}F$ and we will use the following notations: $\tilde{\theta}_{Fi} = \tilde{\theta}(\epsilon_F - \epsilon_i)$, $\tilde{\delta}_{Fi} = \tilde{\delta}(\epsilon_F - \epsilon_i)$, and $\tilde{\delta}^{(1)}_{Fi} = \frac{\partial}{\partial x}\tilde{\delta}(x)\Big|_{\epsilon_F-\epsilon_i}$. Taking the third order derivative with respect to a generic parameter λ of equation 2.20 we obtain:

$$E_v^{(3)} = \sum_i \{(\frac{d^2}{d\lambda^2}\tilde{\theta}_{Fi})\epsilon_i^{(1)} + 2(\frac{d}{d\lambda}\tilde{\theta}_{Fi})\epsilon_i^{(2)} + \tilde{\theta}_{Fi}\epsilon_i^{(3)}\} + \frac{d^3}{d\lambda^3}\left\{E_I[n] - \int \frac{\delta E_I[n]}{\delta n(\mathbf{r})} n(\mathbf{r}) d\mathbf{r}\right\} \quad (2.30)$$

From ordinary perturbation theory applied to the Shrödinger equation $H|\psi_i\rangle = \epsilon_i|\psi_i\rangle$, it can be demonstrated that:

$$\begin{aligned}
\epsilon_i^{(1)} &= \langle\psi_i^{(0)}|H^{(1)}|\psi_i^{(0)}\rangle \\
\epsilon_i^{(2)} &= \langle\psi_i^{(0)}|H^{(2)}|\psi_i^{(0)}\rangle + 2\langle\psi_i^{(0)}|H^{(1)}|\psi_i^{(1)}\rangle \\
\epsilon_i^{(3)} &= \langle\psi_i^{(0)}|H^{(3)}|\psi_i^{(0)}\rangle + 6\langle\psi_i^{(1)}|H^{(1)} - \epsilon_i^{(1)}|\psi_i^{(1)}\rangle + \\
&\quad 3\langle\psi_i^{(1)}|H^{(2)}|\psi_i^{(0)}\rangle + 3\langle\psi_i^{(0)}|H^{(2)}|\psi_i^{(1)}\rangle
\end{aligned} \quad (2.31)$$

The first variation of the charge density is:

$$n^{(1)}(\mathbf{r}) = \sum_i \{(\frac{d}{d\lambda}\tilde{\theta}_{Fi})|\psi_i(\mathbf{r})|^2 + \tilde{\theta}_{Fi}[\psi_i^*(\mathbf{r})\psi_i^{(1)}(\mathbf{r}) + cc]\} \quad (2.32)$$

Thus using 2.31 and 2.32, equation 2.30 becomes:

$$E_v^{(3)} = \int H^{(3)}(\mathbf{r})n(\mathbf{r})d\mathbf{r} + 3\int H^{(2)}(\mathbf{r})n^{(1)}(\mathbf{r})d\mathbf{r} + \frac{d^3}{d\lambda^3}\left\{E_I[n] - \int \frac{\delta E_I[n]}{\delta n(\mathbf{r})} n(\mathbf{r}) d\mathbf{r}\right\} + K \quad (2.33)$$

where

$$\begin{aligned}
&K = \\
&\sum_i \{6\tilde{\theta}_{Fi}\langle\psi_i^{(1)}|H^{(1)} - \epsilon_i^{(1)}|\psi_i^{(1)}\rangle + (\frac{d^2}{d\lambda^2}\tilde{\theta}_{Fi})\epsilon_i^{(1)} - (\frac{d}{d\lambda}\tilde{\theta}_{Fi})\epsilon_i^{(2)} + 6(\frac{d}{d\lambda}\tilde{\theta}_{Fi})\langle\psi_i^{(0)}|H^{(1)}|\psi_i^{(1)}\rangle\} = \\
&\sum_i \{6\tilde{\theta}_{Fi}\langle\psi_i^{(1)}|H^{(1)} - \epsilon_i^{(1)}|\psi_i^{(1)}\rangle + \tilde{\delta}^{(1)}_{Fi}(\epsilon_i^{(1)} - \epsilon_F^{(1)})^3 + 6(\frac{d}{d\lambda}\tilde{\theta}_{Fi})\langle\psi_i^{(0)}|H^{(1)}|\psi_i^{(1)}\rangle\}
\end{aligned} \quad (2.34)$$

Here and in what follows H refers to the Kohn-Sham self consistent Hamiltonian. Following [60], from the explicit calculation of eq. 2.33 it results:

$$\begin{aligned} E_v^{(3)} &= \int v_{ext}^{(3)}(\mathbf{r}) n(\mathbf{r}) d\mathbf{r} + 3 \int v_{ext}^{(2)}(\mathbf{r}) n^{(1)}(\mathbf{r}) d\mathbf{r} + \\ &+ \int \frac{\delta^{(3)} E_{xc}[n]}{\delta n(\mathbf{r}) \delta n(\mathbf{r}') \delta n(\mathbf{r}'')} n^{(1)}(\mathbf{r}) n^{(1)}(\mathbf{r}') n^{(1)}(\mathbf{r}'') d\mathbf{r} d\mathbf{r}' d\mathbf{r}'' + K. \end{aligned} \tag{2.35}$$

Eventually we have expressed the third variation of the total energy in a form in which it depends only on the first variation of charge density and on the first variation of the Kohn-Sham wavefunctions.

Eq. 2.35 cannot be easily implemented in its present form: we have already shown that it is possible to calculate $n^{(1)}(\mathbf{r})$ in an efficient way both for metals and semiconductors, however since from standard first order perturbation theory

$$|\psi_i^{(1)}\rangle = \sum_{\epsilon_j \neq \epsilon_i} |\psi_j\rangle \frac{\langle \psi_j | H^{(1)} | \psi_i \rangle}{\epsilon_i - \epsilon_j}, \tag{2.36}$$

an explicit calculation of 2.36 requires the knowledge of both valence and conduction wavefunctions, moreover the possibility that the denominator approaches to zero may lead to numerical instability.

To overcome these two difficulties, in the semiconducting case, it has already been shown [65] that eq. 2.34 reduces to:

$$\begin{aligned} K &= 6 \sum_i^v \langle \psi_i^{(1)} | H^{(1)} - \epsilon_i^{(1)} | \psi_i^{(1)} \rangle = \\ & 6 \sum_i^v \langle \psi_i^{(1)} P_c | H^{(1)} | P_c \psi_i^{(1)} \rangle - 6 \sum_{ij}^v \langle \psi_i^{(1)} P_c | P_c \psi_j^{(1)} \rangle H_{ji}^{(1)}, \end{aligned} \tag{2.37}$$

where P_c is the projector on the conduction states, $\sum^v$ is a summation over valence states, and $H_{ij}^{(1)} = \langle \psi_i H^{(1)} \psi_j \rangle$. As shown in Sec. 2.2 DFPT allows direct evaluation of $|P_c \psi_i^{(1)}\rangle$, and in the new form eq. 2.37 can be easily calculated.

The metallic case is slightly different. Let consider an energy $\bar{E} > \epsilon_F + 3\sigma$, where σ is the width of the smearing function $\tilde{\theta}$, in order to separate partially filled states and empty ones, and note that:

$$\begin{aligned} K &= 6 \sum_i \tilde{\theta}_{Fi} \langle \psi_i^{(1)} P_{\bar{c}} | H^{(1)} | P_{\bar{c}} \psi_i^{(1)} \rangle + \\ & +6 \sum_{ij}^{\bar{v}} \frac{\tilde{\theta}_{Fi} \langle \psi_i^{(1)} P_{\bar{c}} | H^{(1)} | \psi_j \rangle H_{ji}^{(1)} - \tilde{\theta}_{Fj} \langle \psi_i | H^{(1)} | P_{\bar{c}} \psi_j^{(1)} \rangle H_{ji}^{(1)}}{\epsilon_{ij}} + \\ & +2 \sum_{ijk}^{\bar{v}} \frac{H_{ij}^{(1)} H_{jk}^{(1)} H_{ki}^{(1)}}{\epsilon_{ij} \epsilon_{jk} \epsilon_{ki}} (\tilde{\theta}_{Fi} \epsilon_{kj} + \tilde{\theta}_{Fk} \epsilon_{ji} + \tilde{\theta}_{Fj} \epsilon_{ik}) + \end{aligned}$$

$$+3\epsilon_F^{(1)}\left\{\sum_{ij}^{\bar{v}}\frac{\tilde{\delta}_{Fi}-\tilde{\delta}_{Fj}}{\epsilon_{ij}}H_{ij}^{(1)}H_{ji}^{(1)}+2\sum_i\tilde{\delta}_{Fi}\langle\psi_i|H^{(1)}|P_{\bar{c}}\psi_i^{(1)}\rangle\right\}+$$
$$+3(\epsilon_F^{(1)})^2(\sum_i\tilde{\delta}_{Fi}^{(1)}H_{ii}^{(1)})-(\epsilon_F^{(1)})^3(\sum_i\tilde{\delta}_{Fi}^{(1)}), \tag{2.38}$$

where $P_{\bar{c}}$ is the projector on the band states with energy $> \bar{E}$, $\sum^{\bar{v}}$ is a summation on states with energy $\leq \bar{E}$, $\epsilon_{ij} = \epsilon_i - \epsilon_j$. Only $|P_{\bar{c}}\psi_i^{(1)}\rangle$, corresponding to $\epsilon_i < \epsilon_F + 3\sigma$, appears in this formula, and this quantity can be calculated within DFPT, as shown in Sec. 2.2. Moreover it can be checked that in eq. 2.38 every term having null or very small denominator have a well defined limit that is finite and explicitly computable. As an example:

$$\lim_{\epsilon_i\to\epsilon_j}\frac{\tilde{\theta}_{Fi}\langle\psi_i^{(1)}P_{\bar{c}}|H^{(1)}|\psi_j\rangle H_{ji}^{(1)}-\tilde{\theta}_{Fj}\langle\psi_i|H^{(1)}|P_{\bar{c}}\psi_j^{(1)}\rangle H_{ji}^{(1)}}{\epsilon_{ij}}=$$
$$-\langle\psi_i^{(1)}P_{\bar{c}}|P_{\bar{c}}\psi_j^{(1)}\rangle H_{ji}^{(1)}\{\tilde{\theta}_{Fi}+\epsilon_i\tilde{\delta}_{Fi}\}+\langle\psi_i^{(1)}P_{\bar{c}}|H^{(0)}|P_{\bar{c}}\psi_j^{(1)}\rangle H_{ji}^{(1)}\tilde{\delta}_{Fi}. \tag{2.39}$$

To summarize the third variation of the total energy has been expressed, even in the metallic case, in a form in which it depends only on quantities that can be obtained from the knowledge of the linear response for a finite number of states of the K-S Hamiltonian.

Chapter 3

Structure and dynamical properties

In this chapter we present our study of low temperature structure and dynamical properties of Be(0001), Be($10\overline{1}0$), and Mg($10\overline{1}0$) surfaces.

Surface-phonon dispersions for these surfaces have been recently obtained by Electron Energy Loss Spectroscopy (EELS) [15, 16, 66, 67]. While good agreement between theory and experiment for Mg was obtained previously [67], early attempts to interpret Be data using bulk truncated models [15] are significantly different from experiment [15, 16, 66], as it is shown in Fig. 3.1, and 3.2. By *bulk truncated model* it is meant a model in which force constants are calculated for the bulk and used also to model the interaction between atoms at the surface. These models give even a qualitative disagreement with respect to the experiment, in particular, in the Be(0001) case, the sign of the Rayleigh wave (RW) dispersion from $\overline{K}$ to $\overline{M}$ point in the surface BZ is incorrectly given by the model calculation. Consequently a fully *ab initio* approach is needed to describe Be surfaces dynamical properties.

Here we show that calculations performed within DFPT [10, 11] are in very good agreement with experiments for all the mentioned surfaces. These results allow the study of the thermal properties within the quasi harmonic approximation, as will be shown in Chap. 4.

3.1 Be and Mg bulk

As a preliminary step, we have computed the structural and lattice-dynamical properties of the bulk metals. Our calculations have been performed within the local-density approximation (LDA) using pseudopotentials and plane-wave (PW) basis sets. Atoms were described by separable pseudopotentials that include non-linear core correction and have been generated so as to optimally reproduce several atomic configurations [68, 69], to enhance transferability. Our basis set included PW's up to a kinetic energy cutoff of 22 Ry, and 16 Ry, for Beryllium and Magnesium respectively. For both materials BZ integrations were performed with the *smearing* technique of Ref. [58] using the Hermite-Gauss smearing function of order one, a smearing width σ=50 mRy, and a 120-points grid in the irreducible wedge of the bulk BZ. Accurate checks have shown that these parameters result in a satisfactory convergence of all the calculated quantities. Values of the total

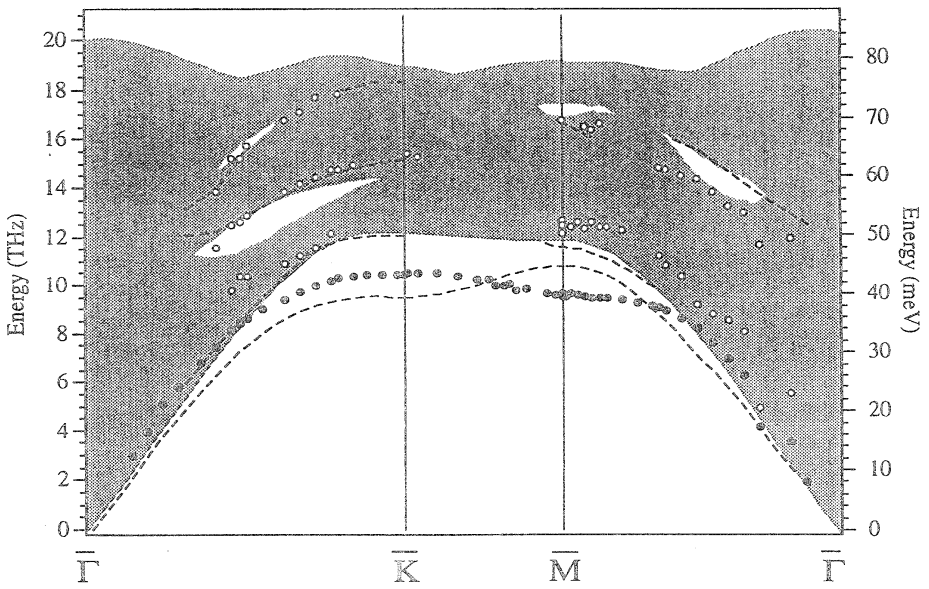

Figure 3.1: Be (0001) surface phonon from EELS [15, 66]. The filled (open) circles indicate intense (weak) features in the measured dispersion. Solid lines indicate the calculated dispersion of surface modes for a bulk-terminated slab. The shaded area corresponds to the projection of bulk phonon modes onto (0001) surface (Fig. from [15]).

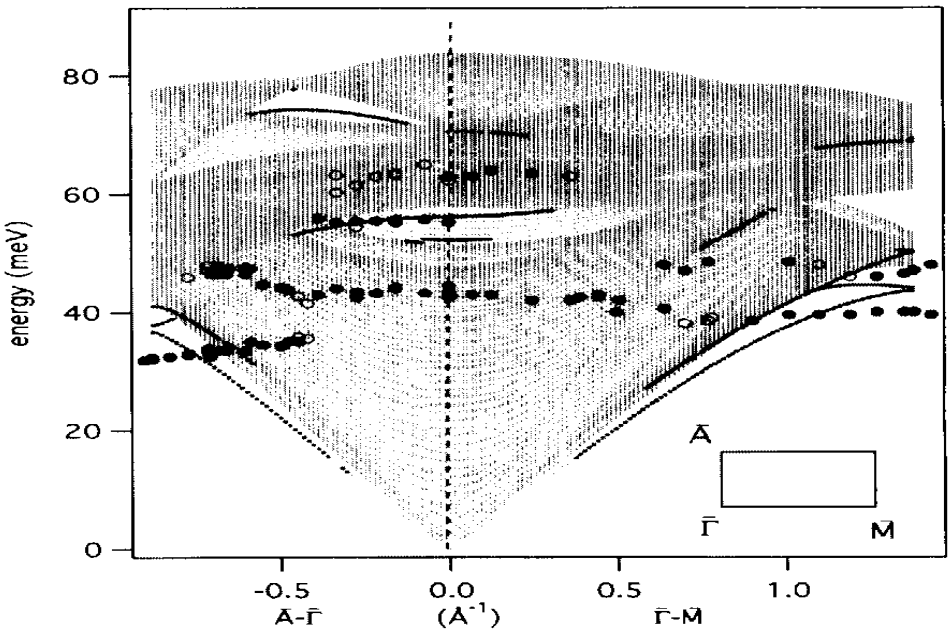

Figure 3.2: Be ($10\bar{1}0$) surface phonon from EELS [16]. The filled (open) circles indicate intense (weak) features in the measured dispersion. Solid lines indicate the calculated dispersion of surface modes for a bulk-terminated slab. The shaded area corresponds to the projection of bulk phonon modes onto ($10\bar{1}0$) surface (Fig. from [16]).

Table 3.1: Comparison between measured and calculated hcp lattice-constants, a and c, bulk modulus, B, and Poisson ratio, ν_P, of bulk Be and Mg.

	a(a.u.)	c/a	B(Mbar)	ν_P
Be(exp.)	4.33	1.568	1.1	0.02-0.05
Be(teo.)	4.25	1.572	1.25	0.04
Mg(exp.)	6.06	1.623	0.35	0.28
Mg(teo.)	5.93	1.629	0.40	0.23

energy calculated at different lattice parameters a, with a fixed c/a, and a fixed kinetic-energy cut-off, have been fitted to a Birch-like equation of state [70]. The equilibrium energy, obtained this way for different c/a, are fitted to a third order polynomial. The resulting equilibrium structural properties are in reasonable agreement with experiments (Tab. 3.1). Note, in the Be case, the contracted value of c/a and the small value of the Poisson ratio, indicating rather strong and anisotropic bonding along the c axis.

In Figs. 3.3, and 3.4 the calculated phonon dispersions of the two bulk materials are displayed and compared with neutron-diffraction data from Refs. [71, 72]. Our calculations are done at the static equilibrium configuration, that is without taking into account lattice expansion due to finite temperature effects. Experimental data for Be are taken at T=80K, and the overall agreement is very good. Data for Mg are taken at T=290K. In Chap. 4 it is shown that, in the case of Magnesium, the agreement greatly improves, considering thermal effects. For Beryllium agreement is slightly worse but still reasonable.

Note that our *ab initio* calculations have *no* adjustable parameter and the only uncontrolled approximations are the adiabatic one and LDA to deal with electronic correlations. The good agreement obtained in the Beryllium case is remarkable, since for this material it is not easy to reproduce accurately experimental data with *empirical* Born-von Karman scheme—as, for instance, in Ref. [15]—even after extensive fitting of the experimental dispersion relations.

3.2 Be (0001) surface

To describe the surface we adopted a repeated slab geometry with 12-layer Be slabs separated by a ≈25 a.u. thick vacuum region (equivalent to 8 atomic layers) to decouple the surfaces. It has been checked that this number of layers is enough to recover bulk properties in the middle of the slab. In the BZ integrations we used a 30-point grid, obtained projecting the bulk grid on the surface BZ. Atomic positions in the slab were fully relaxed starting from the truncated bulk ones, keeping the in-plane lattice parameter fixed at the bulk value. Symmetry fixes atomic in-plane positions and relaxation involves only modification of the inter-layer spacing. The three outmost layers relax significantly from the bulk value, in agreement with experimental evidence [4, 17, 18]. The calculated values for the interlayer spacing variation are reported in Table 3.2, along with experimental data [17] and previous theoretical results. Our theoretical calculation agrees well with previous ones, but all theoretical results disagree with early room-temperature LEED-IV structural

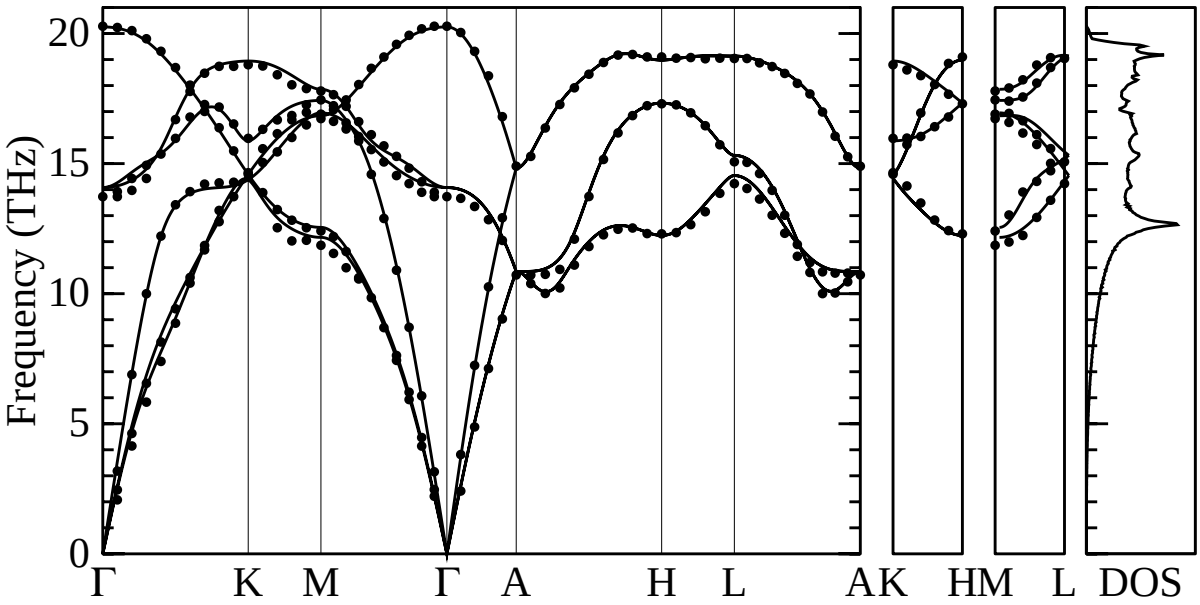

Figure 3.3: Calculated phonon dispersions for bulk Be (lines) and neutron scattering data from Ref. [71] (full dots). The calculated density of states is also shown. Experimental data are taken at T=80K, while theoretical calculations are done at the static equilibrium lattice spacing.

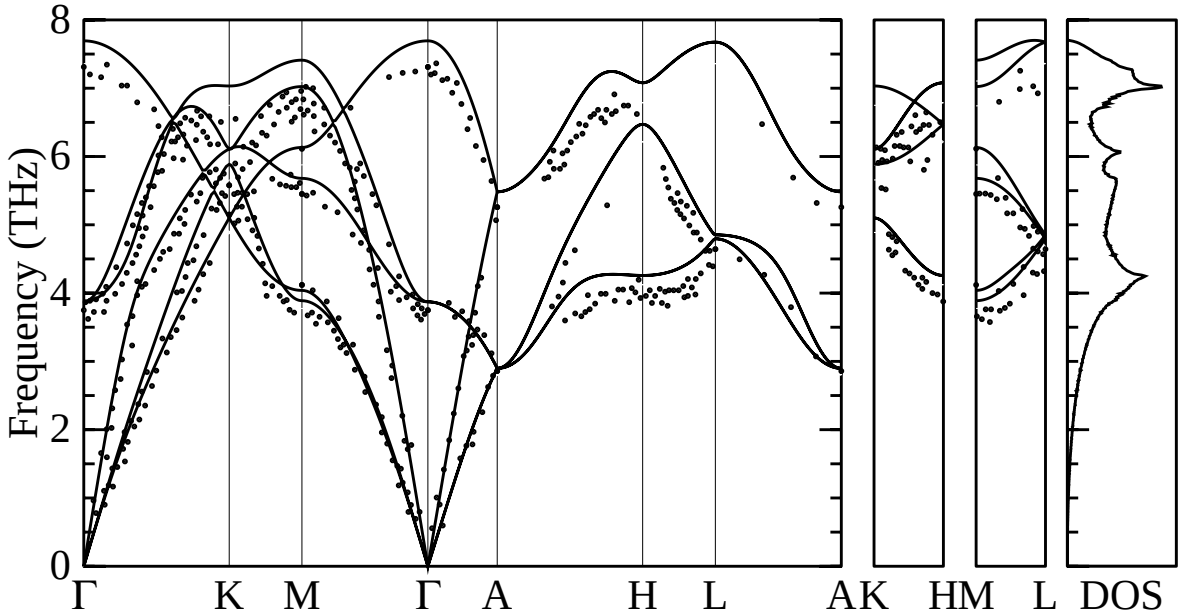

Figure 3.4: Calculated phonon dispersions for bulk Mg (lines) and neutron scattering data from Ref. [72] (full dots). The calculated density of states is also shown. Experimental data are taken at T=290K, while theoretical calculations are done at the static equilibrium lattice spacing.

Table 3.2: Relaxation of the three outer layers of Be (0001) as obtained by LEED and several electronic structure calculations. The experimental temperature is shown, while for the calculations the exchange and correlation functional used and the number of layers in the slab are indicated.

		$\Delta d_{12}(\%)$	$\Delta d_{23}(\%)$	$\Delta d_{34}(\%)$
Exp:	LEED (110 K) [4]	+3.1	+1.4	+0.9
	LEED (300 K)[17]	+5.8	-0.2	+0.2
Th:	LDA-12 layers (this work)	+3.2	+1.0	+0.4
	LDA-10 layers [4]	+2.9	+1.1	+0.4
	LDA-11/13 layers [21]	+2.7	+1.2	+0.6
	LDA-9 layers [19]	+3.9	+2.2	
	GGA-9 layers [22]	+2.5		

determination [17]. The use of different exchange and correlation functionals does not improve the comparison [22]. Recently the importance, in order to get close to LEED results, of including in first-principles calculations the effect of zero-point vibrations has been suggested for transition metal surfaces [6]. In the present case, however, calculation shows (next chapter) that zero-point vibrations do not modify significantly the top layer relaxation.

Very recently a new, low temperature (110 K), LEED-IV determination of the structural properties of Be (0001) surface has been obtained [4]. The agreement between theoretical results and this new experimental determination is very good, the value for the topmost layer expansion being 3.1%, with similar agreement for the inner layers. Disagreement with previous experiments [17] seems to be due to a large extent to a very strong temperature effect [4]. However, first-principles calculation of the surface thermal expansion gives only a relatively small effect, as will be shown in the next chapter.

Real-space interatomic force constants (IFC) of a 12-layer slab were obtained from dynamical matrices, calculated on a 6×6 grid of points in the surface-BZ. Although the surface IFC's are well converged and recover the bulk values in the middle layers of our slab a thicker sample is necessary to decouple those surface vibrations that penetrate deeply in the bulk. The dynamical matrices of a 30-layer slab were built matching the surface IFC's to the bulk ones in the central region, as sketched in Fig. 3.5.

The resulting phonon dispersions, obtained by Fourier interpolation, are reported in Fig. 3.6 together with an indication of the surface character of the calculated modes. Open dots represent modes localized more than 50% in the three topmost layers (dot size is proportional to this percentage), and full dots represent modes localized more than 30% in the topmost layer, and polarized perpendicularly to the surface. It is evident that many layers are involved in the surface dynamics. Comparison in the experiment is shown in Fig. 3.7.

A very good agreement is found between the experimental Rayleigh Wave, the most clearly revealed peaks in the experiment, and the calculated surface vibration that is essentially concentrated in the first layer and polarized perpendicularly to the surface (EELS is a technique particularly sensitive to modes with these characteristics [73]).

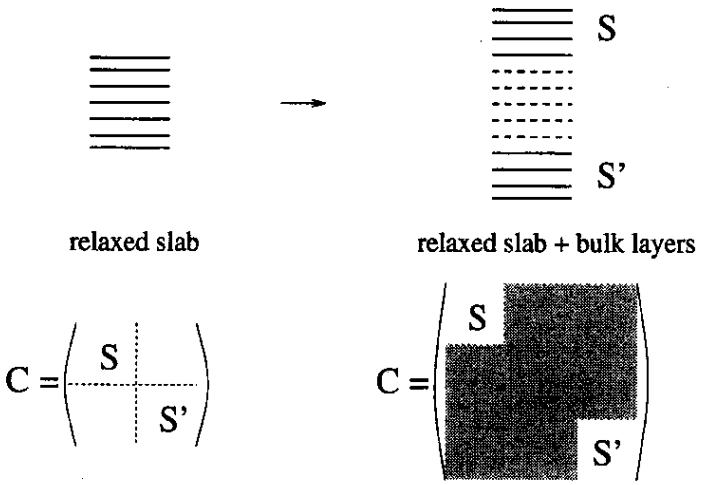

Figure 3.5: Sketch of the procedure used to model the force constant matrix C of a thick slab (on the right). The force constants calculated for a relaxed slab (S blocks) are used to describe the interatomic interaction in the topmost surface layers (solid lines) of a thick slab. Dashed lines indicate bulk layers inserted in order to construct the thick slab. The force constants describing bulk-bulk and bulk-surface interactions are indicated by the shaded blocks, and have been assumed to be equal to the interatomic force constants of the bulk.

However our calculation predicts two additional modes below the bulk-band edge that are not observed in the experiment. These modes are peaked in sub-surface layers and have both in-plane and out-of-plane components. We suggest that they are not observed in the experiment because of the strong intensity of the rather close RW, which, in the region where three modes are predicted, is for more than 70 % localized in the first layer and z-polarized.

Many of the additional surface vibrations in Fig. 3.7 agree qualitatively with weak features present in the experiment (open squares). In particular at the $\overline{M}$ point a shear horizontal mode has been experimentally observed [66] in the appropriate geometry. The experimental value of 50.5 meV agrees well with our result (50.0 meV).

3.3 Be(10$\bar{1}$0) surface

A schematic drawing of the (10$\bar{1}$0) surface of an *hcp* is shown in Fig. 1.4. Two termination are possible, in the Beryllium case the most stable termination is the one with the shortest first interlayer separation [35]. Beryllium (10$\bar{1}$0) surface is more open than the (0001) one and a larger number of layers are involved in the relaxation, thus a larger number of layers is necessary to describe this surface. We have used a 16-layer Be slabs separated by a 6 atomic layers equivalent vacuum region to decouple the surfaces. We used a 32-point grid in the irreducible surface Brillouin zone (SBZ), chosen in order to give a similar density of points as the projection of the bulk grid on the SBZ. Atomic positions in the slab were fully relaxed starting from the truncated bulk, keeping the in-plane lattice parameters

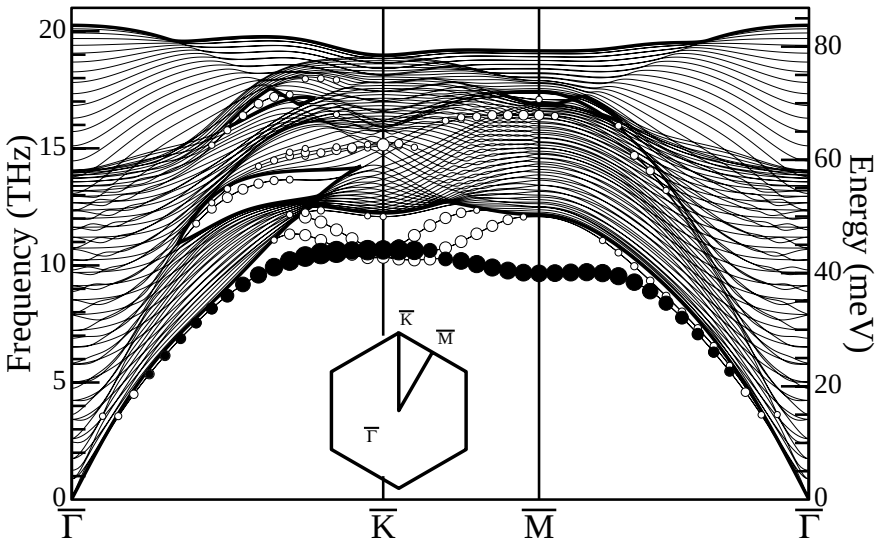

Figure 3.6: Calculated phonon dispersion for a 30-layer slab modeling the Be(0001) surface. Surface modes are represented with dots: modes localized more than 50% in the three topmost layers are shown, and the dot size is proportional to this percentage. Full dots correspond to modes localized more than 30% in the topmost layer and polarized perpendicularly to the surface.

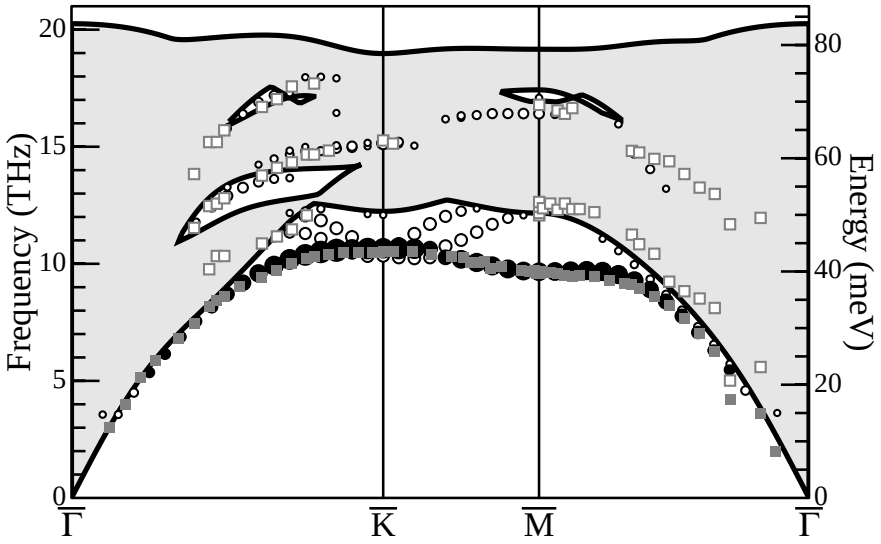

Figure 3.7: Comparison between EELS data from Ref. [15] and calculated surface vibrations of Be(0001) surface. Full and open gray squares correspond to experimental data (intense and weak features, respectively). Dots correspond to calculated modes (see caption of Fig. 3.6). Thick lines delimit the bulk band continuum.

Table 3.3: Relaxation of the four outer layers of Be($10\overline{1}0$) surface, compared with previous electronic structure calculation and experimental LEED results. Experimental errorbar are shown in parenthesis.

	$d_{12}(\%)$	$d_{23}(\%)$	$d_{34}(\%)$	$d_{45}(\%)$
Theory (this work)	-24.5	+6.6	-14.8	+4.7
Theory [35]	-20	+4.4	-13	+3.8
Experiment [35]	-25(-4/+3)	+5(-3/+5)	-11(-5/+8)	+2(-2/+4)

fixed at the bulk value.

The calculated values for the interlayer spacing variation are reported in Table 3.3, along with recent experimental LEED structural data and previous theoretical results [35]. Good agreement is found within experimental errorbar. The numerical values of d_{12} and d_{34} relaxations seem to be very large (-25% and -10% respectively), but it should be kept in mind that they refers to variation of a small quantity: the short interlayer spacing ($d \simeq 1.3$a.u.). Due to Be rather light atomic mass, a precise determination of the bulk and ($10\overline{1}0$) surface structure of Be should take into account also zero point motion. In the next chapter we will show that inclusion of this term does not affect the interlayer relaxation in an appreciable way.

Surface-phonon dispersions of Be ($10\overline{1}0$) were calculated by sampling the SBZ of our 16-layer slab on a 6×4 grid of points and Fourier interpolating dynamical matrices in between to obtain real-space interatomic force constants (IFC). The surface IFC's are well converged and recover the bulk values in the middle layers of the slab. The dynamical matrices of a 104-layer slab were therefore built matching the surface IFC's to the bulk ones in the central region, with the procedure sketched in Fig. 3.5. A thicker slab than the one used to describe (0001) surface is necessary since vibrational modes penetrate more deeply in the bulk.

In Ref. [16] EELS spectra have been taken in the $\overline{\Gamma} - \overline{M}$ and $\overline{\Gamma} - \overline{A}$ directions in the SBZ. Since in both scattering geometries the sagittal plane coincides with a mirror plane of the crystal, vibrations polarized perpendicularly to this plane (shear horizontal modes) cannot be excited [73]. In the following we will call *forbidden* modes those modes that cannot be detected in the experimental configuration used for the corresponding momentum.

In Fig. 3.9 the dispersion of a slab modeling the Be($10\overline{1}0$) surface is shown together with an indication of the surface character of the calculated modes. Dots represent modes localized more than 25% in the three topmost layers (dot size is proportional to this percentage), gray dots represent modes with a polarization forbidden in the scattering geometry used in Ref. [16], and full dots represent modes localized more than 25% in the topmost layer, and polarized perpendicularly to the surface.

Comparison with experiment is shown in Fig. 3.10. The interpretation is straightforward at zone boundaries. At the $\overline{A}$ point only one very pronounced peak is measured (see Fig. 3.8), while three surface modes are predicted by calculation. The two modes at 26.4 and 32.3 meV are mainly polarized perpendicularly to the surface and are concentrated in the second and in the first layer, respectively. The mode localized in the first layer (

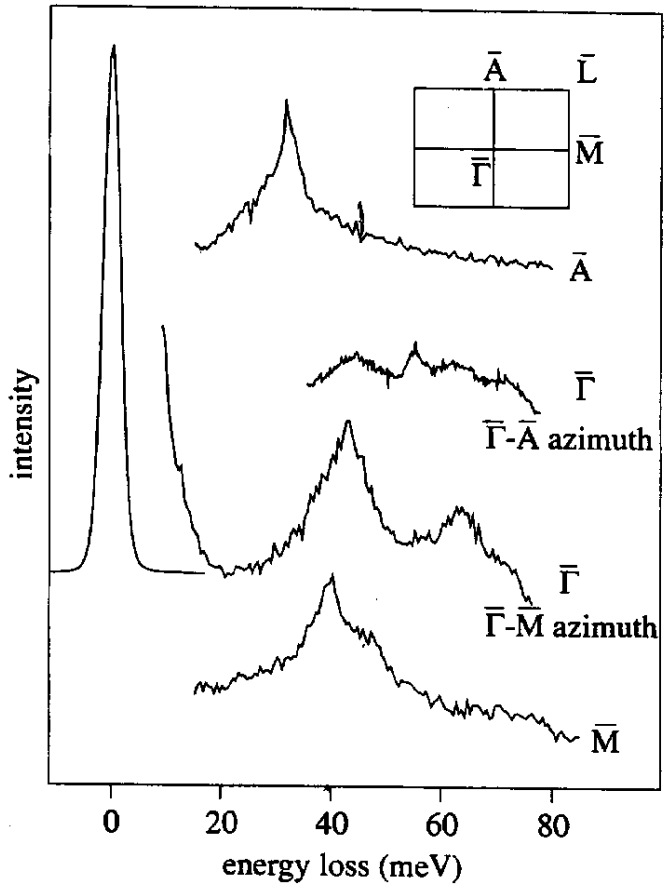

Figure 3.8: Be(10$\bar{1}$0) surface: a set of typical loss spectra taken at the high-symmetry points of the surface Brillouin zone (Fig. from [35])

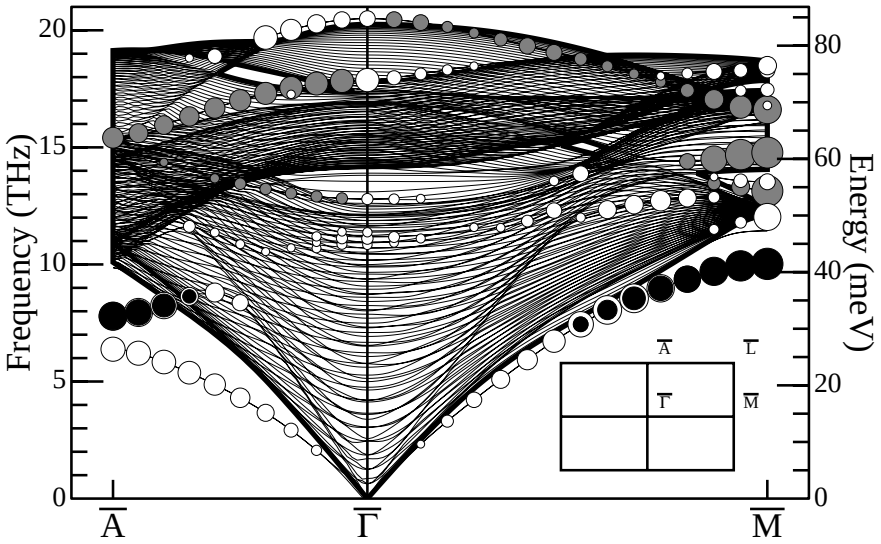

Figure 3.9: Calculated phonon dispersion for a slab modeling the Be($10\overline{1}0$) surface. Surface modes of a 104-layer slab are represented with dots: modes localized more than 25% in the three topmost layers are shown, and the dot size is proportional to this percentage. Gray dots correspond to modes with polarization forbidden in the scattering geometry used in Ref. [16], that is: modes having momentum along the $\overline{\Gamma}-\overline{M}$ ($\overline{\Gamma}-\overline{A}$) SBZ direction and polarized along $\overline{\Gamma}-\overline{A}$ ($\overline{\Gamma}-\overline{M}$) direction are forbidden. Full dots correspond to modes localized more than 25% in the topmost layer and polarized perpendicularly to the surface.

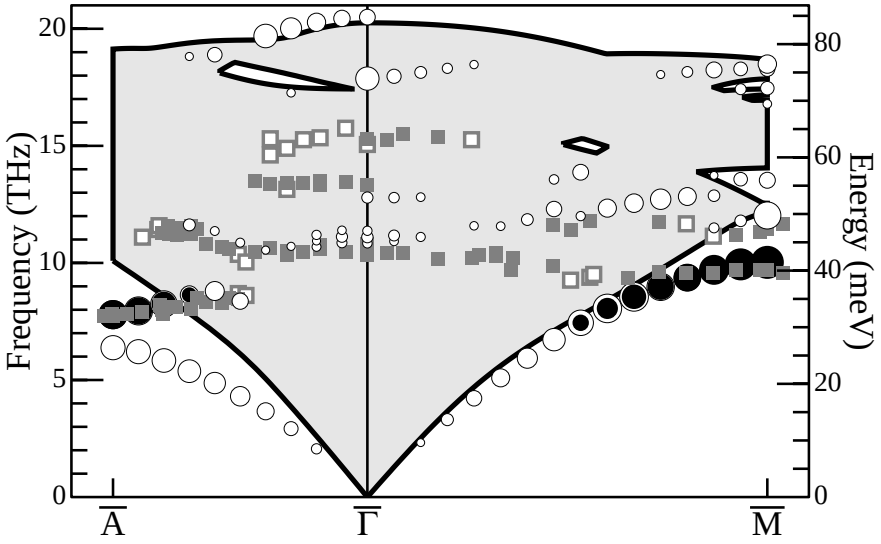

Figure 3.10: Comparison between EELS data from Ref. [16] and calculated surface vibrations of Be($10\overline{1}0$) surface. Full and open gray squares correspond to experimental data (intense and weak features, respectively). Dots correspond to calculated modes (see caption of Fig. 3.9) not forbidden in the scattering geometry used in Ref. [16]. Thick lines delimit the bulk band continuum.

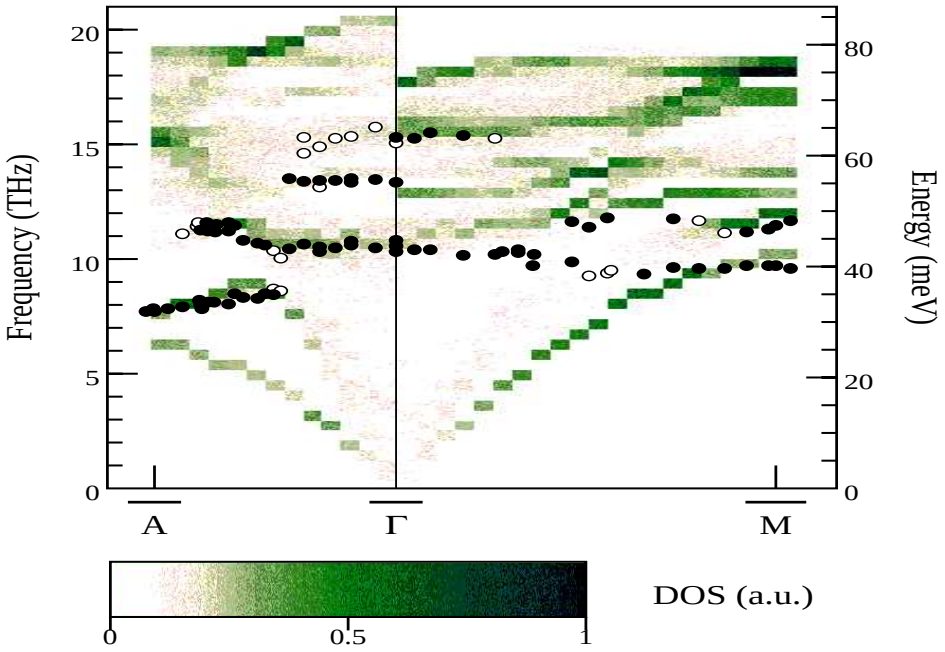

Figure 3.11: Comparison between EELS data from Ref. [16] and calculated vibrational Surface Density of States (SDOS) of Be(10$\bar{1}$0) surface. Full and open dots correspond to experimental data (intense and weak features, respectively). Shaded region represents SDOS. Modes are weighted according to their localization in the 4 outermost layers and symmetry forbidden modes are not considered. Different color correspond to different intensity according to the correspondence reported in the inset.

$\simeq$ 32 meV) reproduces very well the energy and the dispersion of the experimental loss even inside the bulk band edge. Intensity and width of this peak probably mask the other mode, as can be argued from the reported loss spectra [16] shown in Fig. 3.8. The theoretical mode at 63.7 meV is polarized along $\overline{\Gamma} - \overline{M}$ and is thus forbidden. At the $\overline{M}$ point experiment shows two peaks, while calculation finds many modes with different polarizations. There are three calculated modes essentially polarized perpendicularly to the surface at 41.4, 49.8 and 56.0 meV. The first two reproduce very well the two measured losses, the lowest one being essentially concentrated in the first layer and corresponding to the most intense experimental loss.

Again the reported loss spectra [16] shown in Fig. 3.8 suggest that the vicinity of the three modes and the intensity of the first two peaks probably mask the weaker loss at 56.0 meV. Calculation predicts other modes with polarization parallel to the sagittal plane between 69.4 and 76.5 meV, they are less intense and near one to the other, so they probably cannot be separated and are possibly masked by the tail of the Rayleigh wave. Calculation also predicts at 54.3, 61.1 and 68.7 meV three modes with very pronounced surface character but polarized along the $\overline{\Gamma} - \overline{A}$ direction and thus forbidden in the experimental configuration.

At zone center the situation is less clear. Three losses are experimentally observed, measured in the two different scattering geometries (see Fig. 3.8). Among the calculated modes with the most pronounced surface character, one (at 45.9 meV) is polarized perpendicular to the surface and reproduces well the energy and the dispersion of the lowest measured loss. Other calculated modes are polarized in the sagittal plane along the $\overline{\Gamma} - \overline{M}$ (52.9, 73.9 meV) or $\overline{\Gamma} - \overline{A}$ (84.78 meV) directions. These modes are spread on the 5-6 topmost layers, so they probably are not easily detectable by EELS.

In general, surface energy losses may derive not only from excitation of a single mode localized at the surface but also from regions of the bulk spectrum where the vibrational motion at the surface is high due to high vibrational Surface Density of States (SDOS), in spite of the small contribution of each individual mode. From the comparison between experimental data and calculated SDOS (Fig. 3.11) we can associate the experimental loss around 63.3 meV to a zone of high SDOS deriving from the high DOS in the bulk (see Fig. 3.9) and not from large surface contribution of a single mode. Note that at the zone boundaries the Rayleigh wave xsis essentially concentrated in the first layer and gives rise to the most intense losses, thus we think that weak losses deriving from high SDOS can be clearly detected only near zone center.

The third experimentally observed loss at $\overline{\Gamma}$ (at 55.2 meV) does not correspond to any calculated surface mode or resonance of allowed symmetry. From Fig. 3.9 it can be seen that a forbidden mode is actually present in that region of the spectrum. At the present stage we can only speculate that this weak experimental loss might result from a local breaking of the selection rule for the ideal surface [73] due to impurities or roughness probably present at the Be $(10\overline{1}0)$ surface and not included in the calculation.

In conclusion we find that *ab initio* calculations of the vibrational properties of Be $(10\overline{1}0)$ surface reproduce very well the energy and dispersion of many experimentally observed losses. In particular modes polarized perpendicularly to the surface and localized in the first few surface layers compare very well with the most intense experimental peaks

Table 3.4: Relaxation of the four outer layers of Mg(10$\bar{1}$0) surface, compared with previous electronic structure calculation and experimental LEED results, taken at T=120K.

	$d_{12}(\%)$	$d_{23}(\%)$	$d_{34}(\%)$	$d_{45}(\%)$
Theory (this work)	-19.0	+7.9	-10.8	+3.9
Theory [74]	-14.9	+6.9	-7.5	+1.7
Experiment [24]	-16.4	+7.8	—	—

at the zone boundaries.

3.4 Mg(10$\bar{1}$0) surface

As usual to describe the surface we adopted a repeated slab geometry with 16-layer Mg slabs separated by a 6 atomic layers equivalent vacuum region to decouple the surfaces. Using a 24-point grid in the irreducible surface Brillouin zone (SBZ) all calculated properties resuted well converged. Atomic positions in the slab were fully relaxed starting from the truncated bulk, keeping the in-plane lattice parameters fixed at the bulk value. Further details are in Sec. 3.1.

Again many layers are involved in surface relaxation. The calculated values for the interlayer spacing variation are reported in Table 3.4, along with experimental, low temperature, LEED structural data [24] and previous theoretical results [74]. Reasonable agreement is found. Using a slab of 22-layers and a 20 Ry plane wave cut-off results do not change significatively.

Surface-phonon dispersions of Mg (10$\bar{1}$0) were calculated by sampling the SBZ of our 16-layer slab on a 4×2 grid of points and Fourier interpolating dynamical matrices in between to obtain real-space interatomic force constants (IFC). The surface IFC's are well converged and recover the bulk values in the middle layers of the slab. The dynamical matrices of a 96-layer slab were therefore built matching the surface IFC's to the bulk ones in the central region (see Fig. 3.5). Dispersion is shown in Fig. 3.12 together with an indication of the surface character of the calculated modes. Dots represent modes localized more than 30% in the three topmost layers (dot size is proportional to this percentage). Full dots represent modes localized more than 25% in the topmost layer, and polarized perpendicularly to the surface.

Good agreement is found between measured losses and the calculated Rayleigh wave dispersion (Fig. 3.13). Comparing the two analogous Be(10$\bar{1}$0) and Mg(10$\bar{1}$0) surfaces, it is remarkable that the dispersion in the $\overline{A} - \overline{\Gamma}$ direction, of the mode confined in the first layer has different sign in the two materials.

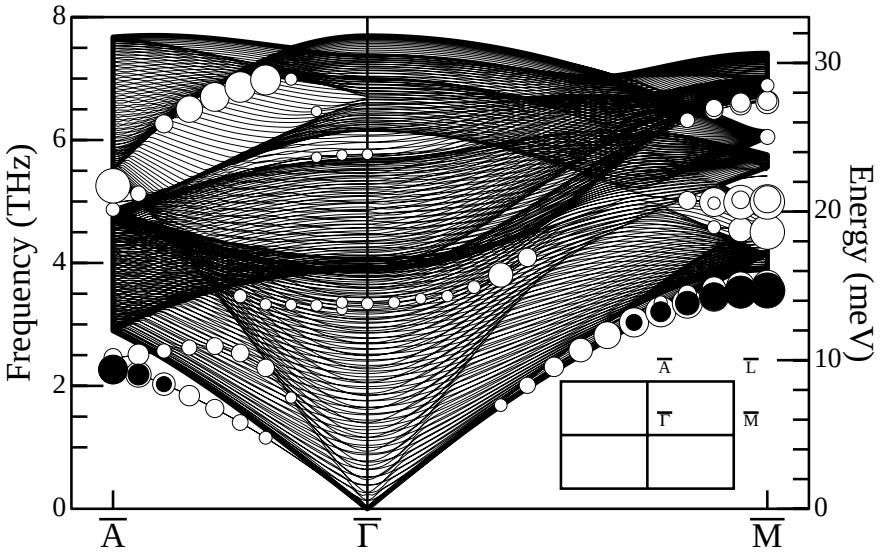

Figure 3.12: Calculated phonon dispersion for a 96-layer slab modeling the Mg($10\bar{1}0$) surface. Surface modes are represented with dots: modes localized more than 30% in the three topmost layers are shown, and the dot size is proportional to this percentage. Full dots correspond to modes localized more than 25% in the topmost layer and polarized perpendicularly to the surface.

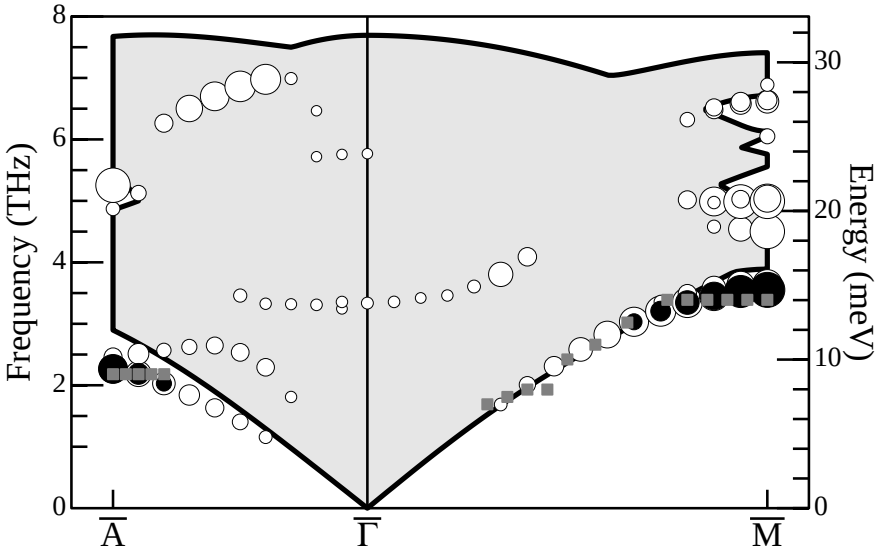

Figure 3.13: Comparison between EELS data from Ref. [67] (gray dots) and calculated surface vibrations of Mg($10\bar{1}0$) surface. Dots correspond to calculated modes (see caption of Fig. 3.12). Thick lines delimit the bulk band continuum.

Chapter 4

Thermal expansion

In this chapter we present a first-principles study, within the quasi harmonic approximation, of the thermal behaviour of Be(0001), Be($10\overline{1}0$), and Mg($10\overline{1}0$) surfaces.

Our calculation describes well the thermal expansion for the bulk materials and has been checked against first-principles molecular dynamics simulations in the (0001) surface case. We do not find the large (0001) surface thermal expansion recently observed experimentally [4] and we argue that the morphology of the actual surface could be less ideal than assumed.

In the case of Be(0001) only one layer is, essentially, involved in the relaxation, and the study of the thermal expansion, has been done by direct derivation of the vibrational free energy. The more complex Be and Mg ($10\overline{1}0$) cases, where many layers are involved in the expansion, have been studied calculating the third order variation of the total energy, with the method described in Chap. 1. In both ($10\overline{1}0$) surfaces QHA predicts negative thermal expansion of the first interlayer spacing, though surfaces as a whole expand. This behaviour has been recently experimentally observed at Mg($10\overline{1}0$) surface [24].

4.1 Be and Mg bulk

In this section the thermal expansion of bulk Be and Mg in the *hcp* structure is studied within the QHA scheme. The structural properties shown in Chap. 3, were instead obtained minimizing only the static energy, $E^{tot}(\mathbf{a})$ in eq. (1.10).

For the *hcp* structure the QHA free energy is a function of the two axis lengths, a and c, and has been calculated from first principles on a grid of points in the two-parameter space. The vibrational contribution to the free energy resulted to be remarkably linear in the two parameters in both materials. Due to low atomic number of Be and Mg, the contribution of zero-point vibrations is expected to be more important than in other systems, especially for Beryllium, and in fact it results in an increase in both lattice parameters of $\approx 0.7\%$ in Be and $\approx 0.3\%$ in Mg. The agreement with experimental data is thus further improved (see Tab. 4.1).

The calculated temperature variations of the bulk lattice parameters are reported, together with available measurements, in Figs. 4.1, and 4.2. From this comparison we conclude that QHA accounts well for Be and Mg bulk anisotropic thermal expansion in

Table 4.1: *hcp* Be and Mg bulk lattice constants. Comparison between experiments(exp.) and calculations done at static equilibrium(static) or including zero-point effects within the Quasi Harmonic Approximation (QHA).

	Be		Mg	
	a	c/a	a	c/a
static	4.25	1.572	5.93	1.629
QHA	4.28	1.571	5.95	1.629
exp.	4.33	1.568	6.06	1.623

the whole temperature range of interest. It is remarkable that in the case of Beryllium c/a ratio contracts increasing the temperature, while in the case of Magnesium it expands, and that this feature is correctly reproduced by the calculation.

In Figs. 4.3, 4.4 we compare bulk phonon measurements taken at finite temperature (T=80 for Be, T=290 for Mg), and already shown in Figs. 3.3, 3.4, with theoretical dispersion obtained at the calculated lattice structures corresponding to the experiment temperature. In the case of Magnesium the agreement between experiment and theory is greatly improved, while for Beryllium the agreement becomes slightly worse, still remaining inside the typical errors obtainable with DFPT.

4.2 Be (0001) surface

Recently a large thermal expansion of the Be(0001) top layer (reaching 6.7% at 700 K) has been experimentally observed [4]. This result was somehow unexpected, since surface phonons show no sign of enhanced anharmonicity [4, 15], however the calculation of the surface thermal expansion [4], within a simplified quasiharmonic approach recently introduced in Ref. [6, 34], resulted in very good agreement with experiments. In Ref. [4, 6, 34] the sum over vibrational modes in the vibrational part of the free energy is replaced by the sum over only three "representative wave packets" corresponding to modes at the surface BZ center where the top layer moves on a rigid substrate, and the validity of such an approach has been criticized by some authors [5]. We have decided to check the accuracy of this approximation [23].

4.2.1 Our calculation

The thermal expansion of the first surface-layer has been calculated by minimizing the QHA free-energy as a function of the first interlayer separation, d_{12}. The vibrational free-energy is calculated summing over a 75×75 regular grid in the surface BZ and over all the vibrational branches of a 30 layers slab, obtained Fourier interpolating dynamical matrices calculated on a 6×6 grid (further details are given in sec. 3.2).

In-plane lattice parameter, $a_{||}$, and all other interatomic distances were assumed to vary according to the calculated bulk thermal expansion. In order to evaluate the free energy variation with respect to d_{12} and $a_{||}$, full phonon dispersions have been calculated for two different values of d_{12}, corresponding to *i)* static lattice equilibrium and *ii)* the

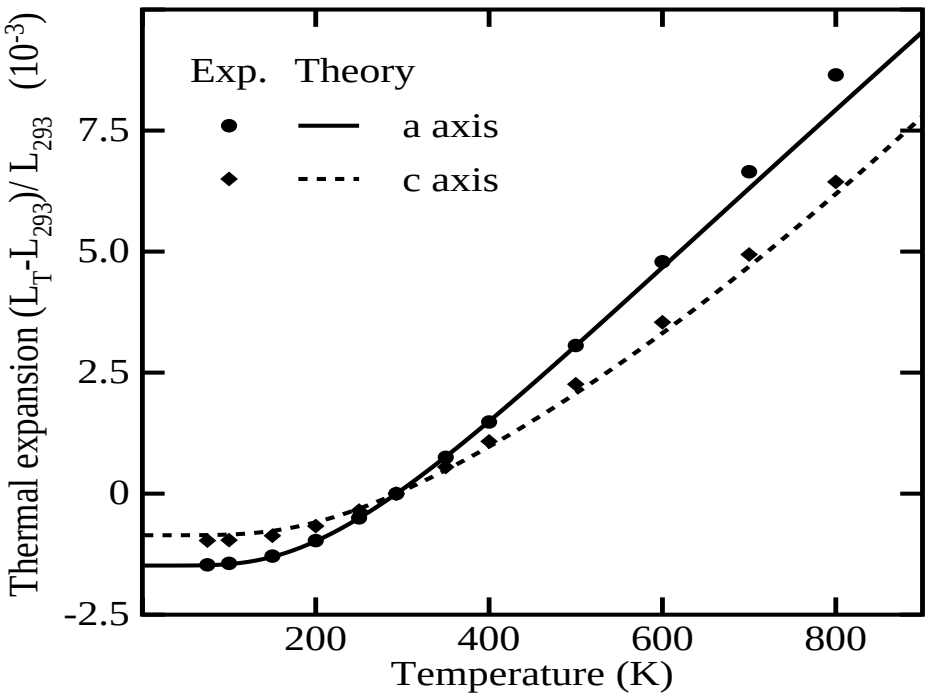

Figure 4.1: Be bulk anisotropic thermal expansion: comparison between experimental data from Ref. [29] and calculation performed within the quasi harmonic approximation. For a comparison: Be bulk Debye Temperature = 1440K, Melting Temperature= 1623K.

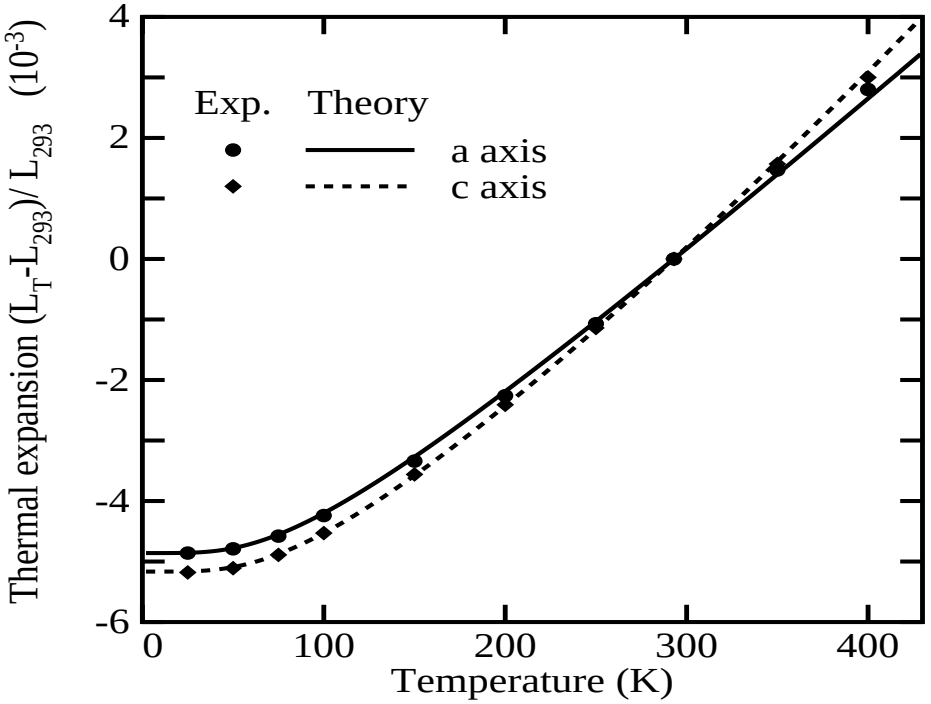

Figure 4.2: Mg bulk anisotropic thermal expansion: comparison between available experimental data from Ref. [29] and calculation performed within the quasi harmonic approximation. For a comparison: Mg bulk Debye Temperature = 400K, Melting Temperature= 924K.

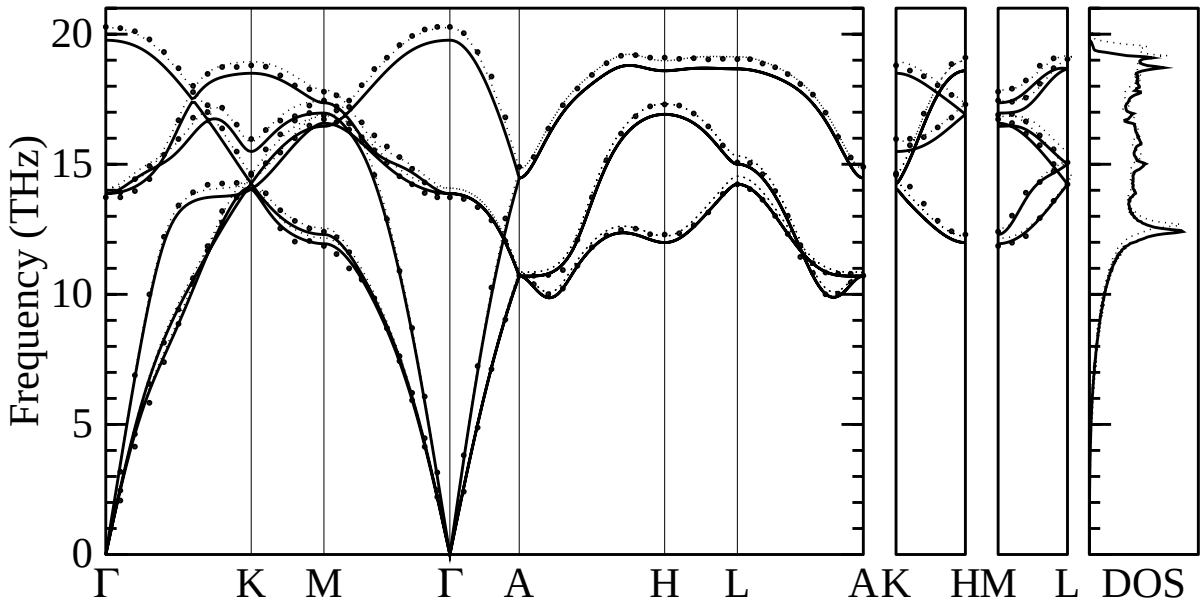

Figure 4.3: Be bulk phonon dispersion: comparison between neutron scattering data taken at T=80K from Ref. [71] (full dots), and theoretical phonon dispersions calculated at the static equilibrium lattice spacing ($a = 4.25$a.u., $c/a = 1.572$, dashed lines) and at the calculated lattice spacing corresponding to T=80K ($a = 4.28$a.u., $c/a = 1.571$, continuous lines).

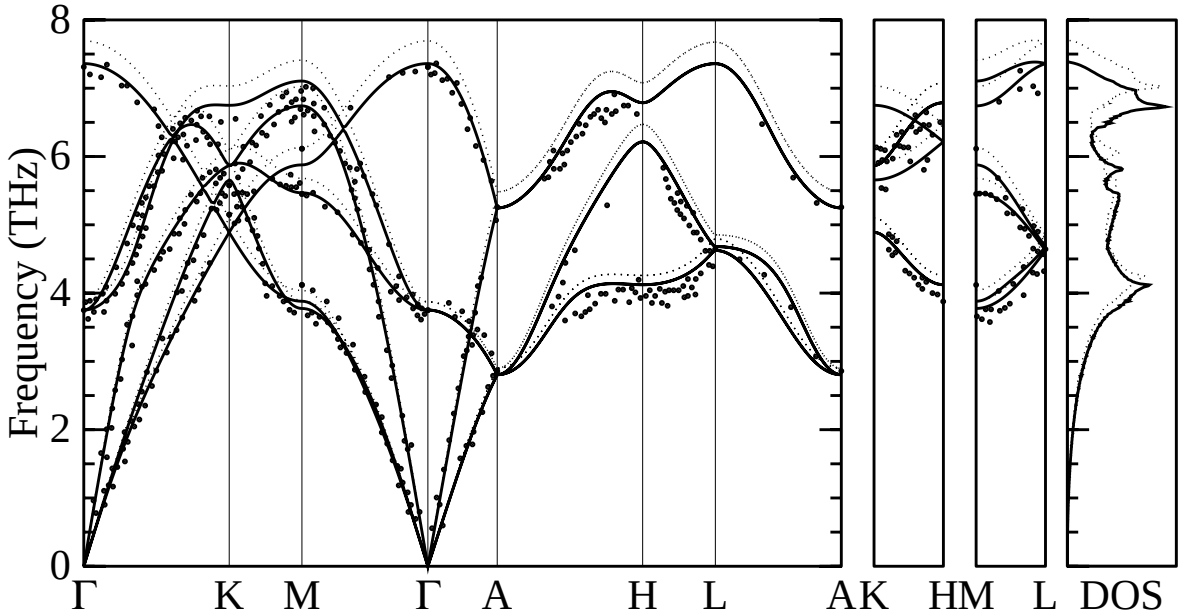

Figure 4.4: Mg bulk phonon dispersion: comparison between neutron scattering data taken at T=290K from Ref. [72] (full dots), and theoretical phonon dispersions calculated at the static equilibrium lattice spacing ($a = 5.93$a.u., $c/a = 1.629$, dashed lines) and at the calculated lattice spacing corresponding to T=290K ($a = 5.98$a.u., $c/a = 1.629$, continuous lines).

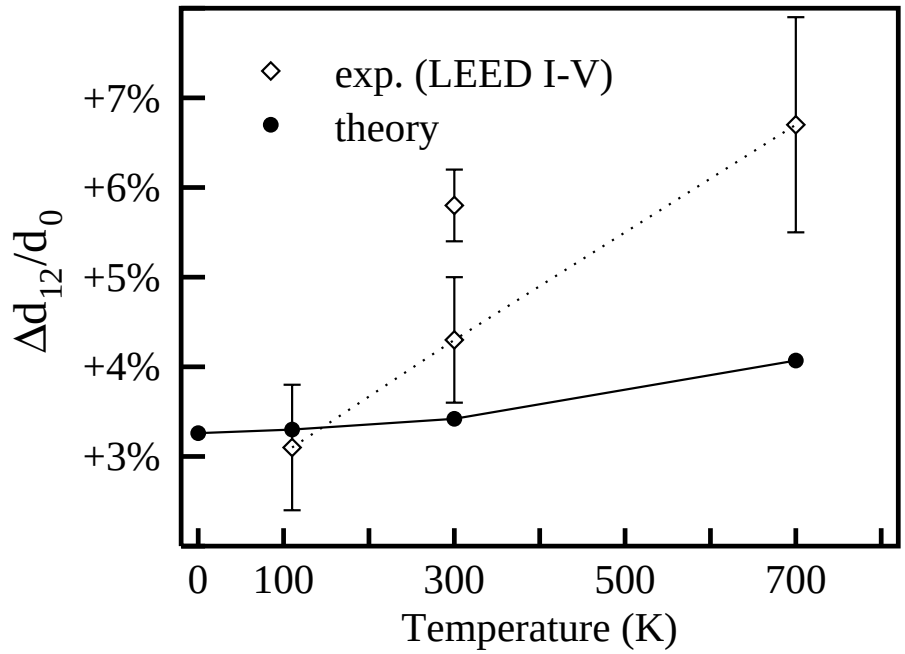

Figure 4.5: Be (0001) surface toplayer expansion: comparison between measurements and calculation done within the quasi harmonic scheme. The upper experimental point at room temperature is from Ref. [17], all other from Ref. [4].

topmost layer further expanded by 2%, and two in-plane lattice parameters, corresponding to *i)* static equilibrium geometry and *ii)* the theoretical bulk value at T =700 K ($a = 4.31$ a.u.). The resulting vibrational free energies were interpolated (bilinearly) in between.

We have examined the effect of varying the second interlayer spacing on our results and found that they are unaffected by its precise value: varying $\Delta d_{23}/d_0$ between 0 and 1.5% the total energy of the slab as a function of d_{12} does not change neither minimum position nor its curvature.

Our results are reported in Fig. 4.5 along with experimental data [4, 17]. Zero-point motion does not change significantly the first interlayer distance at zero temperature (3.3%) with respect to the static result (3.2%). By increasing the temperature the topmost layer relaxes outward reaching 4.1% expansion, relative to the corresponding bulk value, at 700 K. At all temperatures, the expansion is mainly due to anharmonicity in the out-of-plane vibrations that accounts for about 90 % of the effect. On the contrary the large thermal expansion calculated in Ref. [4] with the "three mode samplig" is due to softening of the in-plane "vibrations". Good agreement with experimental data is found at the lowest temperature as well as "reasonable" disagreement at room temperature, in view of the scatter between experimental data, mainly due to different experimental analysis [4]. At the highest temperature, however, the discrepancy is well beyond the experimental errorbar.

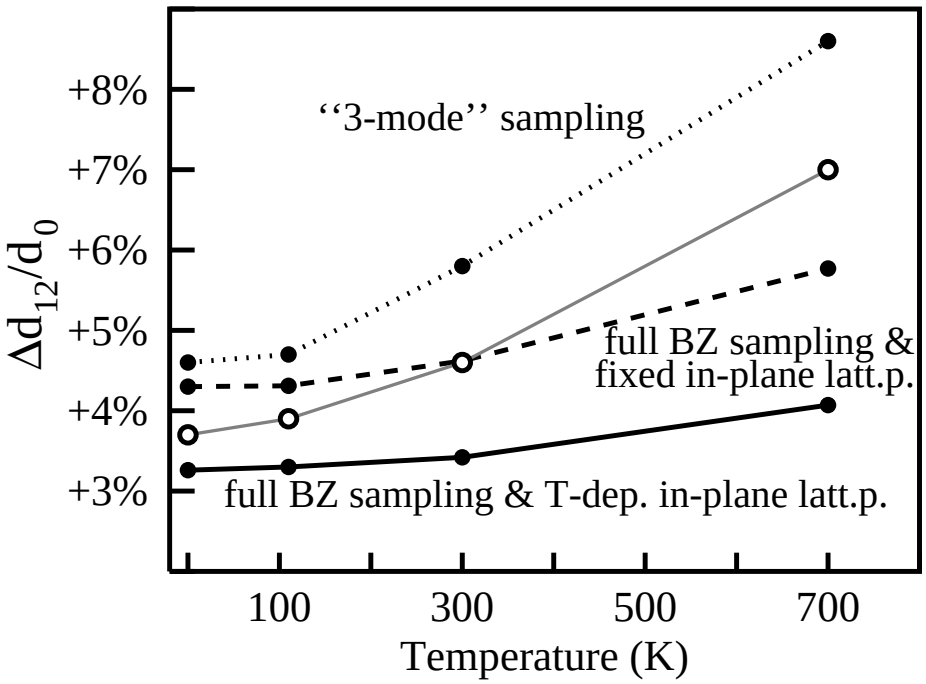

Figure 4.6: Be (0001) surface: first layer thermal expansion calculated at various levels of approximation (full dots and lines, see text) compared with theoretical results from Ref. [4] (open circles).

4.2.2 Comparison with previous theoretical results

Since in Ref. [4] very good agreement has been obtained with experimental data using the simplified QHA approach introduced recently in Ref. [6, 34], we tested the validity of this approach in the present case. In Ref. [4, 6, 34] the sum over vibrational modes in the vibrational part of the free energy is replaced by the sum over three "representative wave packets" corresponding to modes at the surface BZ center where the top layer moves on a rigid substrate. Moreover the in-plane lattice parameter is kept fixed at all temperatures.

In Fig. 4.6 we report the results of calculations at various degrees of approximation (full dots) together with the theoretical results from Ref. [4] for comparison (open circles). The lowest curve (full line) is our most accurate result, already shown in Fig. 4.5. Keeping fixed the in-plane lattice parameter at the static equilibrium value, still performing the full summation over vibrational modes in the free energy calculation, results in an almost rigid outward shift of the top layer (dashed line). This is a trivial effect associated with the zero-point motion tendency to make the system to expand. No large thermal effect is observed. It is only when the accurate sampling of the vibrational mode is drastically reduced to include only the three "representative wave packets" that a large (spurious) thermal effect appears in the calculated interlayer separation (dotted line), very similar to the results obtained with the same approximation in Ref. [4] (open circles). A similar, although less dramatic, overestimation of the surface thermal expansion due to the three-modes approximation [6, 34] has also been found for Ag (111) surface [75].

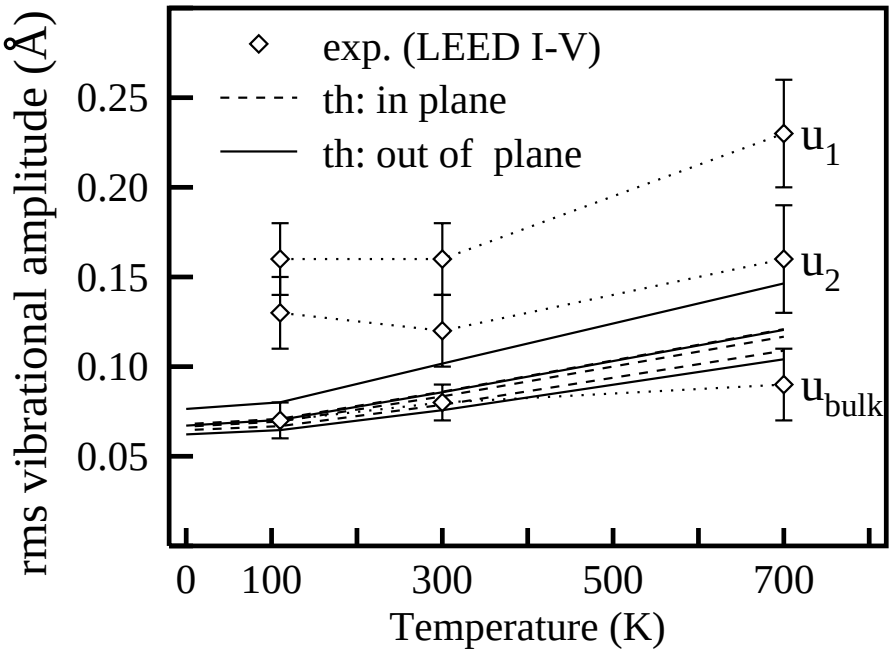

Figure 4.7: Be (0001) surface: comparison between experimental [4] and theoretical root mean square vibrational displacements. Results for the first two layers and for the bulk are shown: outer layers display larger rms amplitudes. Theoretical values are shown for vibrations perpendicular (continuous lines) and parallel (dashed lines) to the surface and display some amount of anisotropy in the topmost layer. In the experimental analysis isotropic vibrations were assumed.

4.2.3 Comparison with the experiments

In the previous section we conclude that, in the case of Be (0001) surface, the better the calculation the worse is the agreement with the experiment. This failure might suggest that QHA itself is inadequate at high temperature, due to the enhanced anharmonicity at the surface [76] with respect to the bulk case, where QHA works well. Comparison of experimental and theoretical root mean square (rms) vibrational displacements also shows (Fig 4.7) good agreement for the bulk values, over the whole temperature range of interest, while for the two topmost surface layers experimental rms displacements appear to be much larger than theoretical ones. Note, however, that enhanced anharmonicity cannot be the (only) reason for these discrepancies. In fact, experimental surface-layer rms values are larger than theoretical ones even at low temperatures where QHA is expected to be accurate and accounts well for the observed surface relaxation. Note also that the *temperature dependence* of the rms displacements is well described by the calculation and the agreement with experiment could be greatly improved by a rigid shift in the theoretical, or experimental, data.

It is well known (see for instance Refs. [77, 78]) that it is very difficult to tell apart static and dynamical displacements in LEED analysis and we believe that Fig. 4.7 carries strong indications that in the actual surface some degree of structural disorder is present, which has erroneously been attributed to dynamical effects. Deviations from *clean* and *flat* morphology would certainly affect the apparent rms displacements, the layer relaxations

Table 4.2: Be (0001) surface layer expansion and out-of-plane (in-plane) rms displacements at 700 K. Comparison between results obtained from FPMD, QHA, and QHA with classical statistics (CQHA).

	FPMD	CQHA	QHA
$\Delta d_{12}/d_0$	+3.7%	+3.8%	+3.6%
$\Delta d_{23}/d_0$	+1.7%	-	-
u_1(Å)	0.15 (0.12)	0.14 (0.12)	0.14 (0.13)
u_2(Å)	0.12 (0.11)	0.11 (0.12)	0.11 (0.12)
u_3(Å)	0.11 (0.11)	0.10 (0.11)	0.10 (0.11)

and their temperature dependence in LEED analysis of "nominally ideal" surfaces. We found, for instance, that a complete *fcc* Be adlayer, whose stacking-fault cost is only 50 meV/atom in LDA, relaxes outward 2% more than the *hcp* terminated surface. Since adatoms are more stable, by $\approx$ 40 meV, in *fcc* sites than in *hcp* ones [21], mixed *fcc/hcp* layers could exist, especially if some residual H, affecting the local energetics of defects [21] were present. More experimental and theoretical work is still needed on this issue.

4.2.4 First principles molecular dynamics

In order to further asses the accuracy of QHA we have performed a first-principles molecular dynamics (FPMD) simulation, where anharmonicity is fully taken into account, studying the system at the highest (700 K) temperature of interest, where the disagreement of QHA results with experimental data is largest and the classical treatment of the atomic motion in FPMD is most reliable. Our FPMD simulation cell consists of 8 atomic layers separated by $\approx$ 4-layer thick vacuum region, with 3×3 in-plane periodicity; in-plane lattice parameter was fixed at the calculated bulk value at $T = 700$ K (4.31 a.u.). Data were taken for about 2 ps in a microcanonical run, with average total kinetic energy corresponding to $T = 700$ K. The result for the interlayer separations and rms amplitudes of the simulation are reported in Table 4.2. The estimated statistical error associated to these results is of a fraction of percent for the interlayer separations and somewhat larger for the rms displacements.

In order to make a direct comparison with QHA results and to check for potential errors associated with the reduced BZ sampling—corresponding to the limited in-plane periodicity in the FPMD simulation—as well as the reduced number of layers and vacuum-layer thickness, the QHA calculation have been redone using the same technical details involved in the FPMD simulation. To display the relevance of quantum effects on the atomic motion at this temperature the calculation have been performed using both quantum statistics, Eq. (1.10), or classical Boltzmann statistic. All these data are gathered in Table 4.2 where it is evident that: *i)* FPMD simulation, consistently with QHA results, shows only a small top-layer expansion at 700 K and rms amplitudes smaller than experimentally reported; *ii)* QHA is perfectly adequate to deal with anharmonic effects in Be (0001) surface at this high temperature; *iii)* classical or quantum statistics makes very little difference at 700 K, of the order of the difference due to reduced BZ sampling and

slabs thickness (our most accurate QHA calculation gives, for instance, a value of 4.1% for the top layer expansion).

In conclusion, from the comparison with FPMD, we find that QHA is well suited to describe thermal properties of Be (0001) surface up to the high temperature experimentally investigated, but results obtained in oversimplified approaches must be handled with care. This is an important result in view of the application of QHA to the study of surface thermal properties of other systems.

Comparison with experiments shows that accurate LDA calculations for the *clean* and *flat* Be (0001) surface cannot explain the large reported first-layer thermal expansion. We argue that the origin of the disagreement should be searched in the morphology of the real surface.

4.3 Be and Mg(10$\bar{1}$0) surfaces

In this section we show our preliminary calculation of the Be and Mg(10$\bar{1}$0) surfaces thermal expansion. Many layers are involved in the thermal expansion and eq. 1.12 has been solved within an *ab initio* approach.

With the scheme of Sec. 2.4 we have calculated derivative of Be and Mg dynamical matrices for a 16-layers slab at the equilibrium positions of the static equilibrium lattice parameters. Details of the calculation are the same as in Chap. 3.

In order to test the separation of the two surfaces of the slab, it has been checked that variation of the dynamical-matrix elements corresponding to atoms of the central layers is negligible, for displacements of the 5 outermost layers, for both materials.

Free energy derivatives with respect to displacements perpendicular to the surface of the 5 outermost layers ($\partial F^{vib}/\partial d_i, i = 1, \ldots, 5$) have been calculated according to eq. 1.14, and results are shown in Fig. 4.8. We have used a 32-layers slab (built as described in Fig. 3.5), and summation was performed on two different grid of q-points, that is the 4 high symmetry points in the surface BZ, or only $\overline{\Gamma}$ and $\overline{\mathrm{M}}$. In the case of Be both grid were used while for Mg only a preliminary calculation on the 2 q-point grid has been done.

From Fig. 4.8 it can be seen that improving the sampling in the case of Beryllium, some of the calculated values change noticeably, however the resulting surface relaxation is only slightly affected. As a consequence we believe that the "4q-points" sampling is accurate enough for the present purpose, and also that our preliminary calculation for Mg gives qualitatively correct results. In the case of Be(0001), where we have performed a very accurate sampling of the modes, we have checked that a summation on an analogous grid indeed gives correct results. Note that the "3-mode" sampling of Ref. [6,34], already addressed in Sec. 4.2.2 considers only the frequencies of three "effective modes" at the zone centre, corresponding to the motion of the first layer on a rigid substrate. On the contrary in our calculations all the modes of a sufficiently large slab are calculated exactly. These results indicate that a correct description of the vibrational modes of the system is crucial, even though the number of q-point used to sample the Brillouin zone is not so critical.

Using the vibrational forces ($\partial F^{vib}/\partial d_i$) so obtained, and solving eq. 1.12 we have

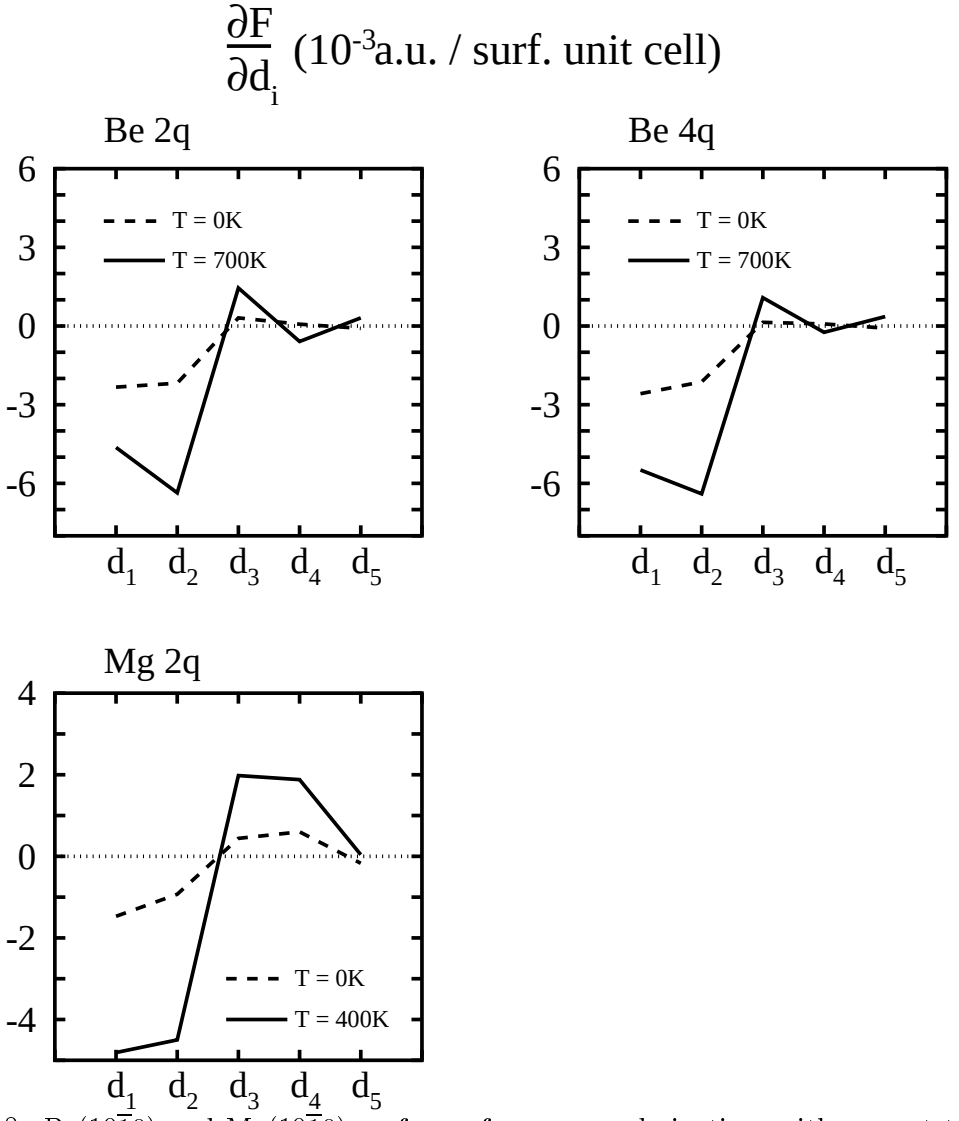

Figure 4.8: Be($10\bar{1}0$) and Mg($10\bar{1}0$) surfaces: free energy derivatives with respect to displacements perpendicular to the surface of the 5 outermost layers ($d_1, \ldots d_5$), at various temperature. Calculation has been performed on a 32-layers slab summing on two different grid of q-points. The labels "4q" and "2q" indicate that summation is done respectively on the 4 high symmetry points in the surface BZ or only on $\overline{\Gamma}$ and $\overline{\mathrm{M}}$.

calculated the thermal expansion of the 4 outermost interlayer spacings ($d_{i,i+1}$). Results are shown in Fig. 4.9 (full lines) together with LEED measurements [24, 35] (open dots). To make a comparison in Fig. 4.9 we also show the expansion obtained relaxing atomic positions at the calculated lattice spacings corresponding to a given temperature, neglecting other thermal contributions (dashed lines), and the static equilibrium lattice spacing results (full dots). Note that while the static contribution leads to an overall contraction, inclusion of entropic terms leads to an overall expansion of the surfaces. At $T = 0K$ zero-point motion does not change appreciably interlayer distances with respect to static results, this is related to the fact that while bulk effects increase the in-plane lattice spacing, thus contracting the surface, surface free energy leads the surface to expand. It is remarkable that in all cases studied (see also Sec. 4.2.1) these two effects cancel each other almost exactly. The overall agreement with experiments is rather good, in particular we have reproduced the negative thermal expansion of the first interlayer spacing at Mg(10$\bar{1}$0) surface, and we predict that the same behaviour should be observed at Be(10$\bar{1}$0) surface.

Results shown in this section are only preliminary for several reasons. Vibrational forces calculated for deeper layers should be included to achieve higher accuracy on d_{45}. Moreover $\{\partial F^{vib}/\partial d_i\}$ have been computed at the equilibrium lattice spacing, and effects due to in-plane lattice expansion should be included also in this part of our calculation, although we expect that, as was the case for the Be(0001) surface, this quantity does not change significantly varying the lattice spacing according to the temperature. Finally the static energy term has been approximated with its second order expansion with respect to the atomic displacements calculated at the equilibrium positions of the expanded lattice spacing corresponding to a given temperature. In conclusion improvements in our calculation are necessary, but we believe that the obtained general behaviour is correct, and reproduces observed results.

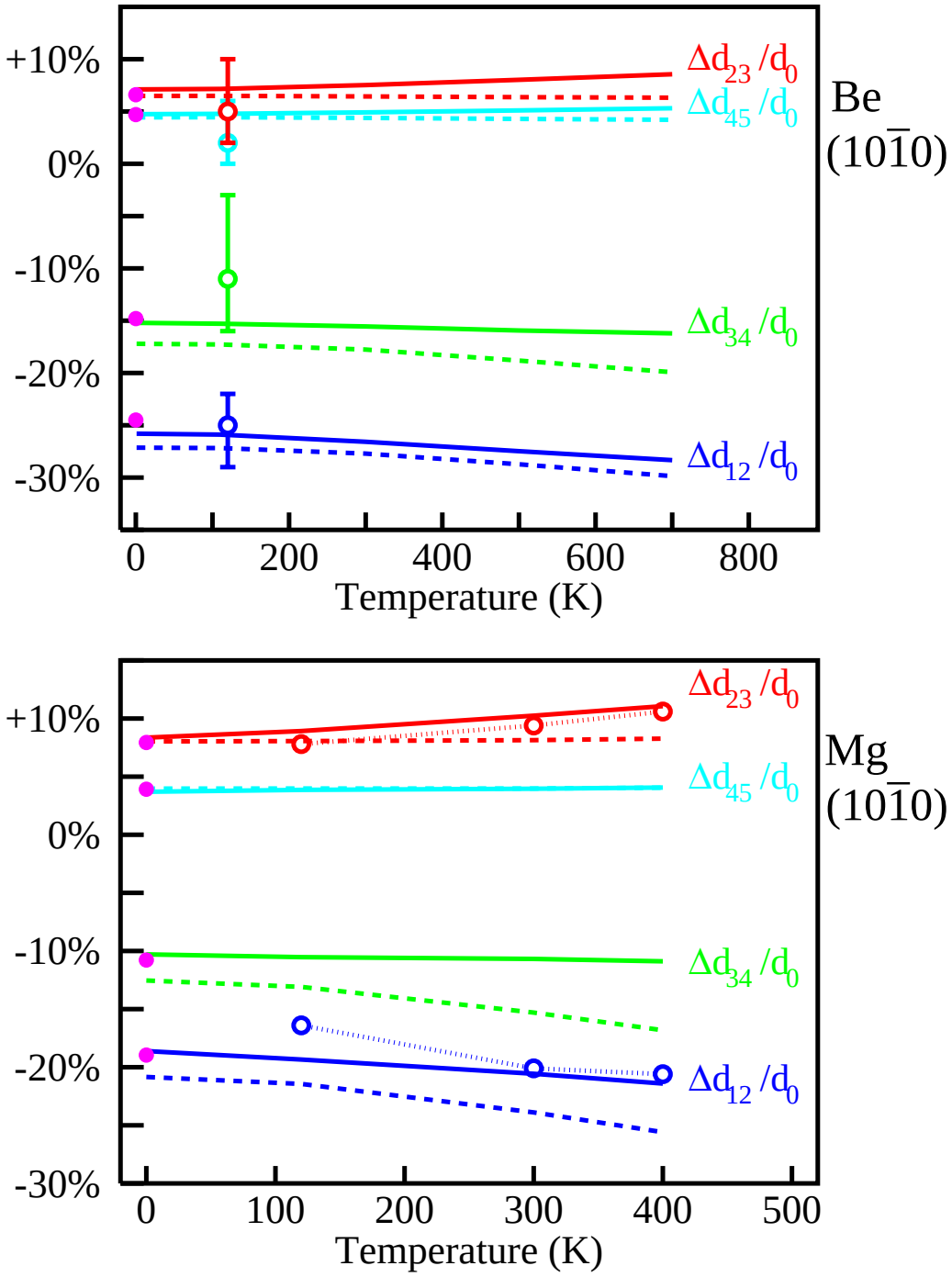

Figure 4.9: Be(10$\bar{1}$0) and Mg(10$\bar{1}$0) surfaces: thermal expansion of the first four interlayer spacings calculated within the quasi harmonic approximation (continuous lines). To make a comparison the expansion obtained with a static calculation at the lattice spacing corresponding to a given temperature is also shown (dashed lines). Full dots correspond to relaxed positions at the static equilibrium lattice spacing. Open dots are LEED measurements from Ref. [24, 35].

Conclusions

The present work has been devoted to the study of the surface thermal expansion within a fully *ab initio* approach. We have investigated the usefulness of the Quasi Harmonic Approximation (QHA) in dealing with surfaces, and we have extended this scheme to systems more complex than those studied so far. In order to do this, a method to calculate analytically third order derivative of the total energy of a metallic system has been implemented within the framework of Density Functional Theory (DFT)[7, 8], and Density Functional Perturbation Theory (DFPT) [10, 11].

Our attention has focused on Be(0001), Be($10\overline{1}0$), and Mg($10\overline{1}0$) surfaces, and for both these simple metals our approach describes very well the low temperature structural and dynamical properties of the bulk material and of the considered surfaces. Only one layer is, essentially, involved in the thermal expansion of the Be(0001) surface, and this system has been studied by direct numerical derivation of the quasi-harmonic free energy. On the contrary a larger number of layers expands in the case of Be($10\overline{1}0$), and Mg($10\overline{1}0$) surfaces, and to study these systems is has been necessary to calculate analytically the free energy derivative with respect to many atomic displacements.

Beryllium (0001) surface has recently attracted much attention because of its measured anomalously large outward relaxation [4]. We have studied Be(0001) surface thermal expansion within the QHA scheme, and we have performed first-principles molecular dynamics simulations. From the comparison of the results obtained with the two approaches we deduce that QHA is well suited to describe thermal properties of the Be(0001) surface up to the high temperature experimentally investigated. We have performed a very accurate sampling of the vibrational modes necessary to calculate quasi-harmonic free energy, and a study of the approximations involved indicates that results obtained in oversimplified approaches [4] are misleading, in this case. We have studied the *clean* and *flat* Be (0001) surface, and we do not find the large thermal expansion experimentally observed, thus we suggest that the origin of the disagreement should be searched in the morphology of the real surface.

Recently a negative thermal expansion of the first interlayer spacing has been experimentally observed for the Mg($10\overline{1}0$) surface [24]. This is one the few cases reported at present, and our preliminary calculation confirms this result, predicting the same effect at the Be($10\overline{1}0$) surface.

Acknowledgments

I want to thank my supervisor Stefano de Gironcoli for his continuous suggestions and for having taught me most of the things I used to complete this work, Stefano Baroni, Raffaele Resta and Erio Tosatti for the pleasant atmosphere created in the Condensed Matter Sector in SISSA. During my work I have been in contact with many persons who have helped me with useful discussions and suggestions, among them I would like to thank Claudia Bungaro, Andrea Dal Corso, Pasquale Pavone, Pietro Ballone, Paolo Ruggerone and Vincenzo Fiorentini. Thanks to Stefano Cozzini, Carlo Cavazzoni and Fanz Di Tolla for their help. Thanks to Stefano Martinelli, Gabriele Cipriani and Lorenzo De Santis for their encouragement and precious suggestions. Thanks to all the friends who have made plesant my stay in SISSA.

Finally I owe my gratitude to Pietro Iseppi for many illuminating discussions we had during my stay in Trieste, and, last but not least, thanks *to Marie* ....

Bibliography

[1] Y. Cao, and E. Conrad, Phys. Rev. Lett. **65**, 2808 (1990).

[2] J.W.M. Frenken, F. Huusen, and J.F. van der Veen, Phys. Rev. Lett. **58**, 401 (1987).

[3] P. Statiris, H.C. Lu, and T. Gustafsson, Phys. Rev. Lett. **72**, 3574 (1994).

[4] K. Pohl, J.-H. Cho, K. Terakura, M. Scheffler, and E.W. Plummer, Phys. Rev. Lett. **80**, 2853 (1998).

[5] A. Kara, P. Staikov, A.N. Al-Rawi, and T.S. Rahman, Phys. Rev. B **55**, R13440 (1997).

[6] J.-H. Cho and M. Scheffler, Phys. Rev. Lett. **78**, 1299 (1997).

[7] P. Hohemberg and W. Kohn, Phys. Rev. **136**, B864 (1964).

[8] W. Kohn and L.J. Sham, Phys. Rev. **140A**, 1133 (1965).

[9] R. Car, and M. Parrinello Phys. Rev. Lett. **55**, 2471 (1985).

[10] S. Baroni, P. Giannozzi, and A. Testa, Phys. Rev. Lett. **58**, 1861 (1987).

[11] P. Giannozzi, S. de Gironcoli, P. Pavone and S. Baroni, Phys. Rev. B **43**, 7231 (1991).

[12] N.R. Werthamer, in *Rare gas solids*, ed. by M.L. Klein, and J.A. Venables (Academic Press, London, 1976).

[13] P. Pavone, S. Baroni, and S. de Gironcoli, Phys. Rev. B **57**, 10421 (1998).

[14] A.A. Quong and A.Y. Liu, Phys. Rev. B **56**, 7767 (1997).

[15] J.B. Hannon, E.J. Mele and E.W. Plummer, Phys. Rev. B **53**, 2090 (1996).

[16] Ph. Hofmann and E. W. Plummer, Surf. Sci. **377-379**, 330 (1997).

[17] H.L. Davis, J.B. Hannon, K.B. Ray, and E.W. Plummer, Phys. Rev. Lett. **68**, 2632 (1992).

[18] L.J. Johansson, H.I.P. Johansson, J.N. Andersen, E. Lundgren, and R. Nyholm, Phys. Rev. Lett. **71**, 2453 (1993).

[19] P.J. Feibelman, Phys. Rev. B **46**, 2532 (1992).

[20] P.J. Feibelman and R. Stumpf Phys. Rev. B **50**, 17480 (1994).

[21] R. Stumpf, and P.J. Feibelman, Phys. Rev. B **51** 13748 (1995).

[22] N.A.W. Holtzwarth and Y. Zeng, Phys. Rev. B **51**, 13653 (1995).

[23] M. Lazzeri, S. de Gironcoli, Phys. Rev. Lett. **81**, 2096 (1998).

[24] Ismail and E.W. Plummer, Bull. Am. Phys. Soc. **43, 1**, 46 (1998).

[25] M.W. Ashcroft and N.D. Mermin, *Solid State Physics* (Saunders College Publishing, New York, 1976).

[26] C. Kittel, *Quantum theory of Solids, (Wiley, New York, 1963).*

[27] H. Hellmann, *Einführung in die Quantenchemie* (Deuticke, Leipzig, 1937); R.P. Feynman, Phys. Rev. **56**, 340 (1939).

[28] C. Kittel, *Introduction to Solid State Physics, 5th ed.* (Wiley, New York, 1976).

[29] *American Institute of Physics Handbook*, edited by D.E. Gray, 3rd ed. (McGraw-Hill, New York, 1972), Table 4e-10 and p. 4-120.

[30] M.Y. Chou, Pui K. Lam and Marvin L. Cohen, Phys. Rev. B **28**, 4179 (1983).

[31] C.M. Bertoni, O. Bisi, C. Calandra and F. Nizzoli, J. Phys. F **5**, 419 (1975).

[32] C.M. Bertoni, V. Bortolani, C. Calandra and F. Nizzoli, Phys. Rev. Lett. **31**, 1466 (1973).

[33] A.P. Roy, B.A. Dasannacharya, C.L. Thaper and P.K. Iyengar, Phys. Rev. Lett. **30**, 906 (1973).

[34] S. Narasimhan and M. Scheffler, Z. Phys. Chem. **202**, 253 (1997).

[35] Ph. Hofmann, K. Pohl, R. Stumpf and E. W. Plummer, Phys. Rev. B **53**, 13715 (1996).

[36] R.O. Jones and O. Gunnarson, Rev. Mod. Phys. **61**, 689 (1989).

[37] R.G. Parr and W. Yang, *Density Functional Theory of Atoms and Molecules* (Oxford University Press, N.Y., 1989).

[38] R.M. Dreizler and E.K.U. Gross, *Density Functional Theory: an Approach to the Quantum Many-body Problem* (Springer, Berlin, 1990).

[39] E.P. Wigner, *Group Theory and Its Application to the Quantum Mechanics of Atomic Spectra* (Academic, New York, 1959), Chap. 5.

[40] M. Buongiorno Nardelli, S. Baroni, and P. Giannozzi, Phys. Rev. Lett. **69**, 1069 (1992).

[41] S. Baroni, P. Giannozzi, and E. Molinari, Phys. Rev. B **41**, 3870 (1990).

[42] S. Baroni, S. de Gironcoli, and P. Giannozzi, Phys. Rev. Lett. **65**, 84 (1990).

[43] S. de Gironcoli and S. Baroni, Phys. Rev. Lett. **69**, 1959 (1992).

[44] J. Fritsch, P. Pavone, and U. Scroeder, Phys. Rev. Lett. **71**,4149 (1993).

[45] S. de Gironcoli, Phys. Rev. B **51**, 6773 (1995).

[46] C. Bungaro, S. de Gironcoli and S. Baroni, Phys. Rev. Lett. **77**, 2491 (1996).

[47] A. Debernardi, S. Baroni, and E. Molinari, Phys. Rev. Lett. 75, 1819 (1995).

[48] J.P. Perdew and Y. Wang, Phys. Rev. B **33**, 8800 (1986).

[49] A.D. Becke, Phys. Rev. A **38**, 3098 (1988).

[50] C. Lee, W. Yang and R.G. Parr, Phys. Rev. B **37**, 785 (1988).

[51] D.R. Hamann, M. Schlüter and C. Chiang, Phys. Rev. Lett. **46**, 1494 (1979).

[52] G.B. Bachelet, D.R. Hamann and M. Schlüter, Phys. Rev. B **26**, 4199 (1982).

[53] G.P. Kerker, J. Phys. C **13**, L189 (1980).

[54] N. Troullier and J.L. Martins, Phys. Rev. B **43**, 1993 (1991).

[55] W.E. Pickett, Comp. Phys. Rep. **9**, 115 (1989).

[56] L. Kleiman and D.M. Bylander, Phys. Rev. Lett. **48**, 1425 (1982).

[57] C.L. Fu, and K.M. Ho, Phys. Rev. B **28**, 5480 (1983).

[58] M. Methfessel and A.T. Paxton, Rev. B **40**, 3616 (1989).

[59] S.G. Louie, S. Froyen, and M.L. Cohen, Phys. Rev. B **26**, 1738 (1982).

[60] X. Gonze and J.P. Vigneron, Phys. Rev. B **39**, 13120 (1989).

[61] M.T. Yin and M.L. Cohen, Phys. Rev. B **26**, 3259 (1982).

[62] H.F. King and A. Komornicki, J. Chem. Phys. **84**, 5645 (1986).

[63] T.S. Nee, R.G. Parr and R.J. Bartlet, J. Chem. Phys. **64**, 2216 (1976).

[64] P. Pulay, J. Chem. Phys. **78**, 5043 (1983).

[65] A. Debernardi, Ph.D. Thesis, Oct. 1995 SISSA, Trieste.

[66] J.B. Hannon, and E.W. Plummer, J. elct. Spect. and Related Phen. **64/65**, 683 (1993).

[67] Ismail, C. Bungaro *private comunication.*

[68] A. Dal Corso, S. Baroni, R. Resta and S. de Gironcoli, Phys. Rev. B **47**, 3588 (1993).

[69] A. Dal Corso, Ph.D. Thesis, Oct. 1993 SISSA, Trieste.

[70] F.D. Birch J. Geophys. Res. **91**, 4949 (1986).

[71] R. Stedman, Z. Amilius, R. Pauli, and O. Sundin, J. Phys. F **6**, 157 (1976).

[72] R. Pynn, and G.L. Squires, Proc. R. Soc. Lond. A. **326**, 347-360 (1972).

[73] H. Ibach and D.L. Mills, *Electron Energy Loss Spectroscopy and Surface Vibrations* (Academic Press, New York, 1982).

[74] J.H. Cho, Ismail, Z. Zhang, and E.W. Plummer, Phys. Rev. B **59**, 1677 (1999).

[75] J.J. Xie, S. de Gironcoli, S. Baroni, and M. Scheffler, Phys. Rev. B **59**, 970 (1999).

[76] R.E. Allen and F.W. de Wette, Phys. Rev. **179**, 873 (1969); R.E. Allen, F.W. de Wette, and A. Rahman, *ibid.* **179**, 887 (1969).

[77] B.S. Itchkawitz, A.P. Baddorf, H.L. Davis, and E.W. Plummer, Phys. Rev. Lett. **68**, 2488 (1992).

[78] A.F. Wright and D.C. Chrzan, Phys. Rev. Lett. **70**, 1964 (1993).